The Thesis Committee for Taewoo Ha
Certifies that this is the approved version of the following thesis:

Analysis of Piezoelectric Thin Film Energy Harvester for Biomedical Application

APPROVED BY
SUPERVISING COMMITTEE:

Supervisor: _____
John X.J. Zhang

Co-Supervisor: _____
Nanshu Lu

Analysis of Piezoelectric Thin Film Energy Harvester for Biomedical Application

by

Taewoo Ha, B.S.; B.S.

Thesis

Presented to the Faculty of the Graduate School of

The University of Texas at Austin

in Partial Fulfillment

of the Requirements

for the Degree of

Master of Science in Engineering

The University of Texas at Austin

May 2014

Abstract

Analysis of Piezoelectric Thin Film Energy Harvester for Biomedical Application

Taewoo Ha, M.S.E.

The University of Texas at Austin, 2014

Supervisors: John X.J. Zhang, Nanshu Lu

The effect of the thickness ratio variation of a unimorph piezoelectric energy harvester to the electric output under bending condition is studied. The harvester forms a blanket with PVDF-TrFE as an energy harvesting layer and Kapton film used as a substrate. The thickness of Kapton is fixed as 25um while the thickness of PVDF-TrFE is varied from 0.5 um to 20um. The voltage, charge and energy output are estimated by numerical and theoretical method under three different bending conditions with fair biomedical model. For all conditions, the Young's modulus ratio changes the optimal point of all outputs.

The effect of surface patterning is studied with regard to the rib-base thickness ratio and the rib-spacing ratio. The voltage and electric energy output falls with the decrease of the base-rib thickness ratio. The charge output rises with the decrease of the base-rib thickness ratio. However, the charge increasing rate is smaller than the voltage decreasing rate. Hence, the electric energy decreasing rate is mostly affected by the

voltage decreasing rate. By changing rib-spacing ratio, the electric energy output of the grated structure can be enhanced. If the piezo-substrate thickness ratio is larger than a specific value, the grated structure is more efficient than the planar structure. A recent study from Ran Liu group asserts that the piezoelectric effect becomes electrostatically stronger at the singularity point of the nano imprinted structure where the bending induced stress is also concentrated. Thereby, the grated structure would enhance the electric energy output of the energy harvester.

Overall, this research will contribute to design optimal thin film energy harvester for biomedical application.

Table of Contents

List of Tables

List of Figures

Chapter 1 : Introduction

In recent decades, the energy efficiency of electronic devices is significantly improved and biomedical electronic devices such as pacemakers and defibrillators as well. Still, these devices require external batteries to be activated. However, the external batteries have comparably large volume than devices and regular exchange is required due to lifetime issue. Furthermore, some batteries may have a safety issue in certain circumstances.

Biomechanical energy harvesters create electric energy from activities of daily living [1]. The Sources of energy is the vibration of organs such as muscle, lung, and heart. The amount of generated energy from the biomechanical energy harvesting device is about mW, which is very small but can alternate conventional batteries for any biomedical and biomechanical devices.

Briefly there are two categories in biomechanical energy harvesting device. One is extracorporeal energy harvesting from muscular movement and the other is intracorporeal energy harvesting from organ motion. Examples of extracorporeal energy harvesting devices are described in the Figure 1.1. The Figure 1.1 a) shows an energy harvesting design with shoes. Placing an electromechanical transducer at the bottom of shoes, the mechanical potential energy of human feet is converted to usable electric energy[2]. The second example described in the Figure 1.1 b) is a device collecting energy from the angular displacement of an ankle[3]. The converted electric energy can be used to activate any wearable electronic devices. Not only from feet and ankles, any

movement or displacement of human body can be a source of the energy with the energy harvesting device.

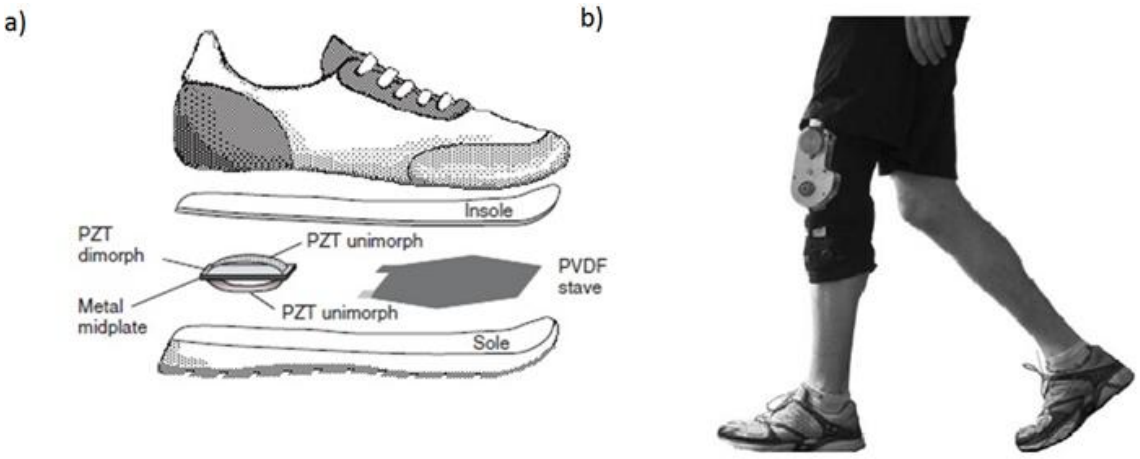

Figure 1.1: Extracorporeal energy harvesting devices. a) Energy harvesting device is placed under a shoe and collect energy from walking. b) Energy harvesting from angular displacement of the human ankle [2, 3].

Unlike extracorporeal devices, intracorporeal devices can be applied to limited situations. There are few moving organs which can be an energy source such as lung and heart, excluding intramuscular implementation. Also the material used in the device should be non-toxic. The stiffness of the device is also critical since most organs are very soft. If a stiff device is attached to the organs, it may inhibit the movement of the organs. The size of device could be an issue since space between organs is restricted.

The Figure 1.2 introduces two intracorporeal devices. The diagram in the Figure 1.2 a) depicts that the energy harvesting implementation can substitute the external battery for pacemakers [4]. The picture in the Figure 1.2 b) shows real implementation of

the energy harvesting device including micro battery [5]. The collected energy is stored into the micro battery so that the energy can be used in specific situations.

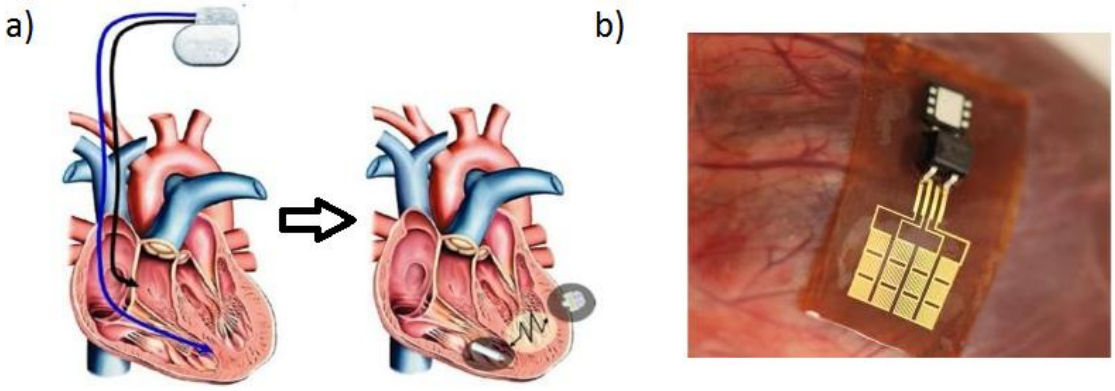

Figure 1.2: Intracorporeal energy harvesting devices. a) The pacemaker battery is no longer required. The collected and stored energy from the cardiac vibration will activate the pacemaker. b) Practical energy harvesting device attached on the epicardiac surface [4, 5].

A key of the electromechanical energy transduce is the material property called piezoelectricity. Some materials have unique crystal structure and dipoles are spontaneously created in the materials due to stress-induced crystal deformation. These materials are called piezoelectric materials. The principles of the piezoelectricity and the kinds of piezoelectric material will be introduced in the chapter 2.

For the biomechanical energy harvesting especially for the intracorporeal devices, the mechanical movement is mostly bending because of the shape of organs and its stiffness. Therefore, the mechanical analysis of the film energy harvesting device under bending condition is important to find the optimal device structure, which is discussed in

the chapter 3. Theoretical and numerical approach proves that there is an optimal thickness ratio between the piezoelectric material and the substrate material under bending condition when two materials form a blanket structure.

The following chapter will introduce additional structure variation to control the electric output of the device. The grated structure is applied to the top surface of the piezoelectric material and the output is numerically analyzed. The analysis asserts that the grated structure geometry variation affects the electric output and it is better than the planar structure in some cases.

Chapter 2 : Piezoelectric Energy Harvesting

In this chapter, general concepts of the piezoelectricity and the working mechanism of the piezoelectric energy harvester are covered. First the piezoelectric effect is described and the piezoelectric coupling coefficients are introduced in Section 2.1. Section 2.1 summarizes different types of piezoelectric materials and their different applications. Section 2.3 focuses on energy harvesters based on piezoelectric materials.

2.1 PIEZOELECTRIC EFFECT

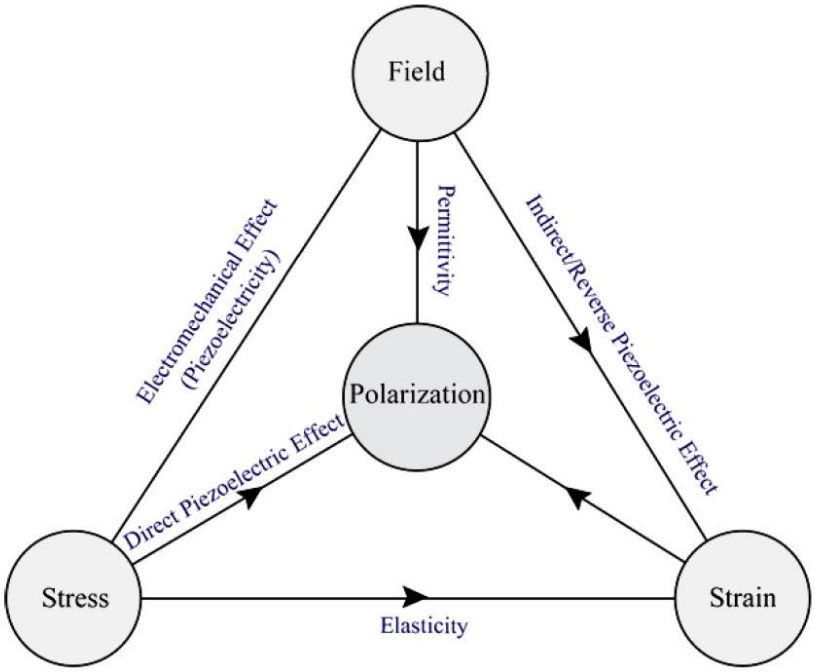

Figure 2.1: A part of Heckmann's diagram for piezoelectric properties.

The origin of the word "piezo" is the Greek, which means "to press." This phenomenon was discovered by Curie [6]. The piezoelectricity can be defined as a direct

conversion between the electric energy and mechanical energy, as described in the Figure 2.1 [7]. Since then, many piezoelectric materials are discovered and used in various applications such as sensors, actuators, sonar, microphones and most famously, lighters. The piezoelectricity in polymers discovered by Kawai broadens the application area where the mechanical flexibility is required [8]. In recent decades, the polymer-based flexible piezoelectric energy harvesting devices are developed in many companies and laboratories. One example is the energy harvesting from organs, as depicted in the introduction chapter; the device attached to organs requires high flexibility.

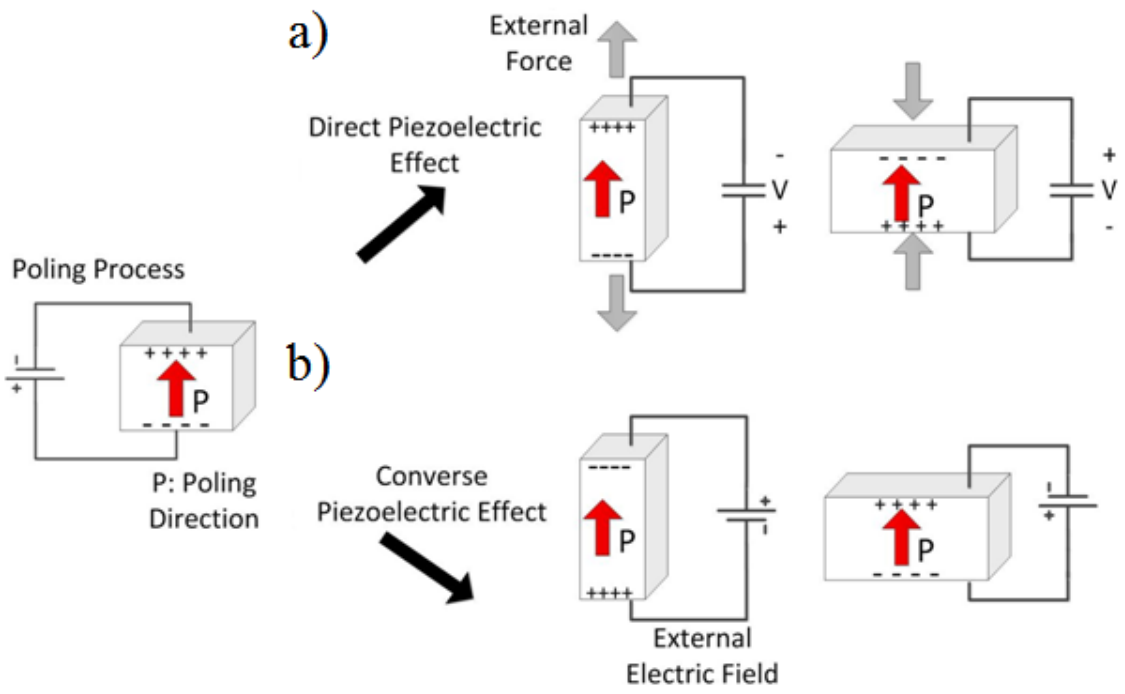

Figure 2.2: a) The direct piezoelectric effect and b) the inverse piezoelectric effect.

The piezoelectric effect is bidirectional, as depicted in the Figure 2.2. The diagram a) in the Figure 2.2 is the direct piezoelectric effect. As can be seen, the polarization is induced by the external tension; hence, the voltage or charge is generated through electrodes. The direct piezoelectric effect can be written as

$$P_T = dT \tag{2.1}$$

Where P_T is the piezoelectric polarization induced by the stress T and d is the piezoelectric coupling coefficient. This direct effect can be used as a sensor or an energy generator [9].

The diagram below is the inverse piezoelectric effect. The interaction between internal polarization tendency and the external electric field from the voltage source deforms the shape of the piezoelectric material. Similarly above, the strain forced by the electric field can be formulated as

$$S_E = d^t E_{in} \tag{2.2}$$

where S_E is the strain induced by the electric field observed in the piezoelectric material E_{in} and d^t is the inverse piezoelectric coupling coefficient. This inverse piezoelectric effect can be applied to any actuator application. The inverse piezoelectric effect is highly frequency-dependent; electrically activated sonar or sound devices are using this effect [10].

The assumption behind Equation (2.1) is there is no external electric field. To generalize the problem, we should define the general electric displacement field for

piezoelectric materials. The electrostatic definition of the electric displacement field induced by the external electric field is given as

$$D = \varepsilon_0 E_{ex} = \varepsilon_0 \varepsilon_r E_{in} = \varepsilon_0 E_{in} + P_E \qquad (2.3)$$

where D is the electric displacement field, E_{ex} is the external electric field, E_{in} is the electric field observed in the dielectric material, P_E is the polarization induced by the external electric field, ε_r is the relative permittivity of the piezoelectric material and ε_0 is the free space permittivity of which the value is $8.854 \times 10^{-12} (\mathrm{F/m})$ [11]. In general electrostatics, the Equation (2.3) denotes the dielectric effect to the electric field. If the external electric field is applied to the dielectric material, the magnitude of electric field decreases because some of the electric field forms polarization.

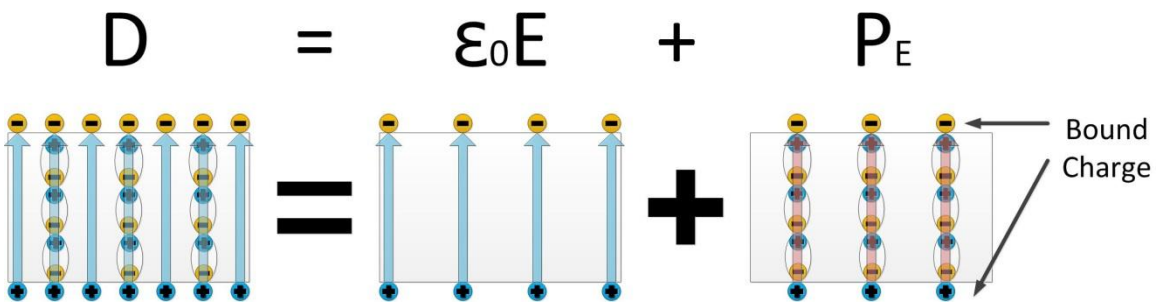

Figure 2.3: The relation among the electric displacement field, electric field and polarization.

Combining the Equation (2.1) and (2.3), the general definition of electric displacement for piezoelectric materials is

$$D = \varepsilon_0 E_{in} + P_E + P_T = \varepsilon_0 \varepsilon_r^T E_{in} + dT \qquad (2.4)$$

where ε_r^T is the relative permittivity under constant stress. Note, the polarization induced by the external electric field P_E and the polarization induced by the stress P_T are different [Ref]. The Equation (2.4) asserts that the electric displacement field of a piezoelectric material can be created by the external electric field or the external mechanical stimulus. If both are applied, the total polarization in the piezoelectric material is the sum of the P_E and P_T, assuming there is no thermal loss.

In a similar manner, the general elastic property of the piezoelectric material can be also formulated. From the Hooke's Law, the relation between the stress and the strain is

$$S_T = sT \tag{2.5}$$

where S_T is the strain derived from the stress and s^E is the compliance coefficient [Ref]. The total strain caused by the stress and the electric field derived from the Equation (2.2) and the (2.5) is

$$S = S_T + S_E = s^E T + d^t E_{in} \tag{2.6}$$

where s^E denotes the elastic compliance coefficient under constant electric field. The Equation (2.6) describes the strain of a piezoelectric material can be caused by the external mechanical stimulus or the external electric field. For the notation unification, the electric field term in the Equation (2.4) and (2.6) is specified with the notation E_{in}, which is the electric field observed in the piezoelectric material. The relation between the external electric field and the internal electric field is $E_{ex} = \varepsilon_r E_{in}$. The electric field notation will be unified as *E* meaning the internal electric field from now on.

The pole direction of the polarization depends on the force direction since the piezoelectric materials are basically anisotropic [7]. This directional nature of piezoelectric materials can be controlled mostly through the pretreatment process called poling process [8]. To describe the anisotropic property analytically, the Equation (2.4) and (2.6) are usually described as tensor.

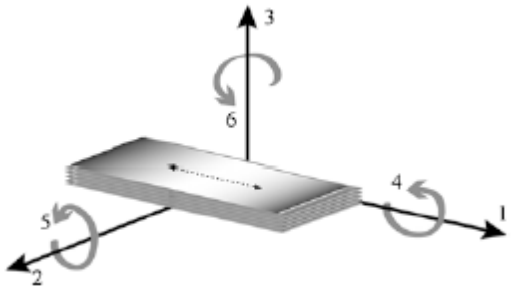

Figure 2.4: Tensor directions in 1-6 numbering system[12].

For convenience, redefinition of the coordinate expression is required; x-x: 11, y-y: 22, z-z: 33, x-y: 12, x-z: 13, y-z: 23. Usually, the numberings are further simplified as described in the Figure 2.4; 11→1, 22→2, 33→3, 23→4, 13→5, 12→6 [12]. This numbering system will be used for the simplicity and the unification from now on. Following the direction numbering notation above, the Equation (2.4) and (2.6) become

$$\begin{bmatrix} D_1 \\ D_2 \\ D_3 \end{bmatrix} = \begin{bmatrix} d_{11} & d_{12} & d_{13} & d_{14} & d_{15} & d_{16} \\ d_{21} & d_{22} & d_{23} & d_{24} & d_{25} & d_{26} \\ d_{31} & d_{32} & d_{33} & d_{34} & d_{35} & d_{36} \end{bmatrix} \begin{bmatrix} T_1 \\ T_2 \\ T_3 \\ T_4 \\ T_5 \\ T_6 \end{bmatrix} + \varepsilon_0 \times \begin{bmatrix} \varepsilon_{r11}^T & \varepsilon_{r12}^T & \varepsilon_{r13}^T \\ \varepsilon_{r21}^T & \varepsilon_{r22}^T & \varepsilon_{r23}^T \\ \varepsilon_{r31}^T & \varepsilon_{r32}^T & \varepsilon_{r33}^T \end{bmatrix} \begin{bmatrix} E_1 \\ E_2 \\ E_3 \end{bmatrix} \tag{2.7}$$

$$\begin{bmatrix} S_1 \\ S_2 \\ S_3 \\ S_4 \\ S_5 \\ S_6 \end{bmatrix} = \begin{bmatrix} s_{11}^E & s_{12}^E & s_{13}^E & s_{14}^E & s_{15}^E & s_{16}^E \\ s_{21}^E & s_{22}^E & s_{23}^E & s_{24}^E & s_{25}^E & s_{26}^E \\ s_{31}^E & s_{32}^E & s_{33}^E & s_{34}^E & s_{35}^E & s_{36}^E \\ s_{41}^E & s_{42}^E & s_{43}^E & s_{44}^E & s_{45}^E & s_{46}^E \\ s_{51}^E & s_{52}^E & s_{53}^E & s_{54}^E & s_{55}^E & s_{56}^E \\ s_{61}^E & s_{62}^E & s_{63}^E & s_{64}^E & s_{65}^E & s_{66}^E \end{bmatrix} \begin{bmatrix} T_1 \\ T_2 \\ T_3 \\ T_4 \\ T_5 \\ T_6 \end{bmatrix} + \begin{bmatrix} d_{11} & d_{12} & d_{13} \\ d_{21} & d_{22} & d_{23} \\ d_{31} & d_{32} & d_{33} \\ d_{41} & d_{42} & d_{43} \\ d_{51} & d_{52} & d_{53} \\ d_{61} & d_{62} & d_{63} \end{bmatrix} \begin{bmatrix} E_1 \\ E_2 \\ E_3 \end{bmatrix} \tag{2.8}$$

2.2 PIEZOELECTRIC MATERIALS

There are many kinds of piezoelectric materials and those materials have different piezoelectric properties. Since applications are under various conditions, required parameters in each application are also different. For example, high dielectric constant and mechanical strength are essential to speakers. For biomedical applications, high

flexibility is one of the most important properties. Table 2.1 shows the piezoelectric properties of classified materials in terms of the molecular structure.

Molecular Structures	Materials	$d_{33}(d_{31})$ [pC/N]	g_{33} $[10^{-3}Vm/N]$	Elastic Stiffness [GPa]	Relative Dielectric Constant
Single Crystal	Quartz ZnO CdS $LiTiO_3$	5-12 (2-7)	57.8	120-200	~10
Polycrystalline	PZTs $BaTiO_3$ Perovskites	60~120 (-40~110)	12.6-42	63	800-1200
Polymer	PVDF P(VDF-TrFE) TGS	-30~-35 (10~25)	380	3	8-12

Table 2.1: Piezoelectric material properties in terms of molecular structure [7, 13-15].

Most single crystal materials such as Quartz, Rochelle salt and tourmaline are naturally created piezoelectric materials. Quartz(SiO_2) structure is in periodic tetrahedron shape, oxygen atoms around a silicon atom [16]. Molecular dipoles caused by electrically dissimilar atoms are balanced due to the symmetric structure. However, the deformation

of the structure caused by external mechanical stimuli breaks the balance; hence spontaneous polarizations are generated inside material, which is direct piezoelectric effect, and vice versa. Zinc Oxide (ZnO) is one of the commonly used synthetic ceramic single crystal materials. ZnO is optically transparent and has wurtzite crystal structure as described in the Figure 2.5 a). The origin of the piezoelectricity of ZnO despite the low dielectric property is its non-centrosymmetric structure, as depicted in the Figure 2.5 b). The piezoelectric performance principle is similar to Quartz, as shown in the Figure 2.5 c). The deposition of ZnO is well defined using physical vapor deposition and chemical vapor deposition. Usually single crystal piezoelectric materials have low piezoelectric coupling property and their elastic stiffness is relatively large. Therefore, single crystal piezoelectric materials are limited in terms of usable power [15].

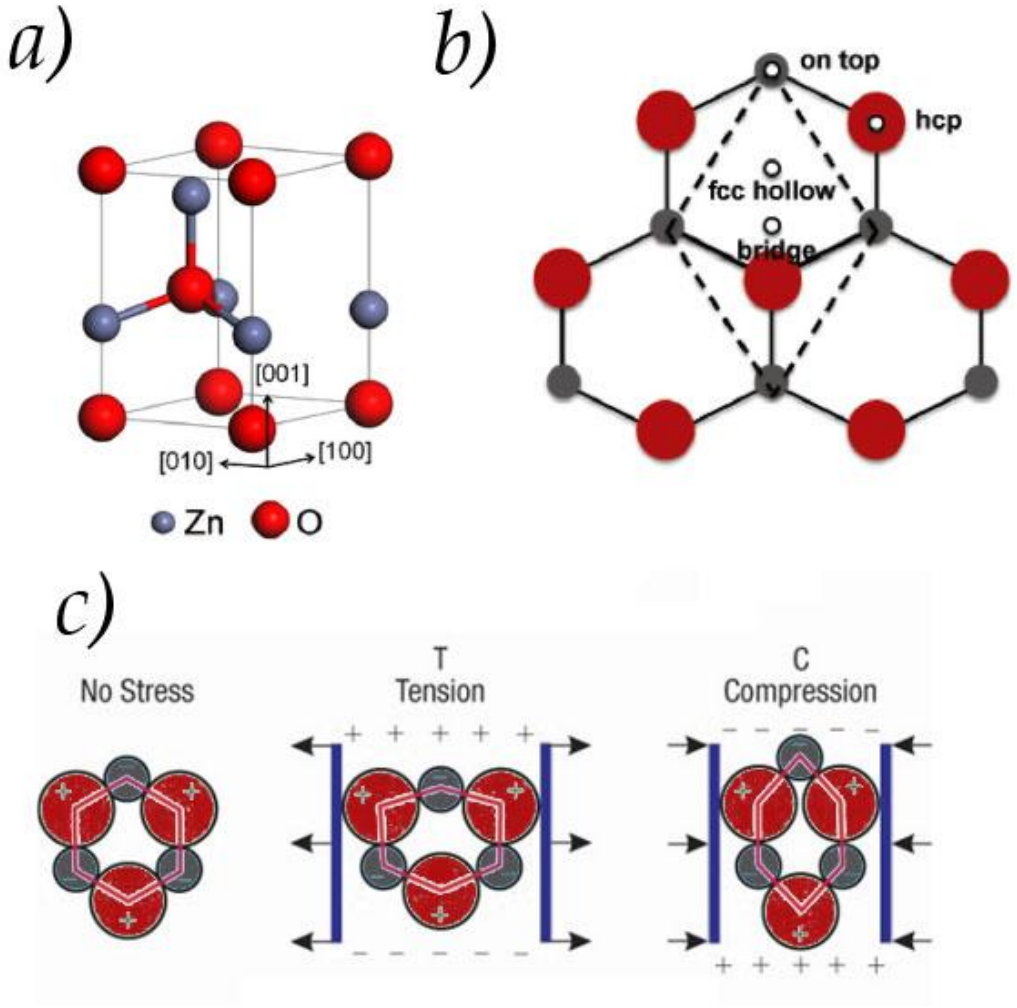

Figure 2.5: Schematics of the piezoelectricity of Zinc Oxide. a) Crystal structure of ZnO (wurtzite ZnO unit cell). b) Hexagonal structure (O-terminated wurtzite ZnO surface) c) Direct piezoelectric principle of ZnO [17].

Polycrystalline piezoelectric materials are commonly used materials in many piezoelectric applications. It has fairly high piezoelectric coefficient and dielectric constant. The elastic stiffness is also usually smaller than single crystal materials unless the structure is very thin. Because of its comparable advantage, polycrystalline

piezoelectric materials such as PZTs, $CaTiO_3$ and $BaTiO_3$ are widely used for actuator applications.

The Figure 2.6 shows traditional perovskite crystal structure. Most polycrystalline piezoelectric materials have perovskite structure. The diagram in the Figure 2.6 a) shows the symmetric cube state of the peroveskite piezoelectric material structure. As the temperature below the Curie point, the lattice becomes asymmetric like the diagram in the Figure 2.6 b). The dipole moment caused by this asymmetry is the origin of the piezoelectricity of the perovskite structure.

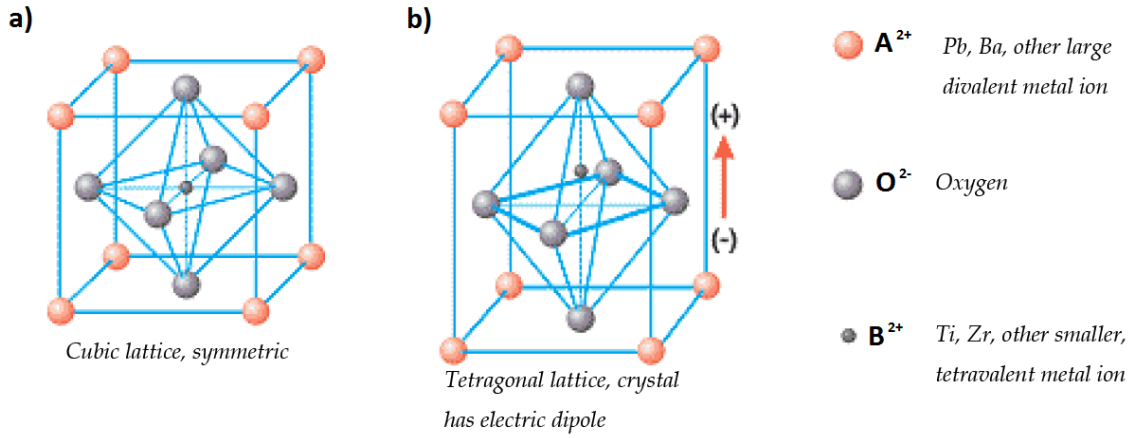

Figure 2.6: Crystal structure of a piezoelectric ceramic. a) Above a Curie point temperature. b) Below the Curie point. [15].

The direction of dipoles in a polycrystalline material is random. Thus, dipoles mostly canceled out in the material. By applying high voltage across the material, those dipoles are aligned and the elongated polarization tendency remains permanently, as described in the Figure 2.7.

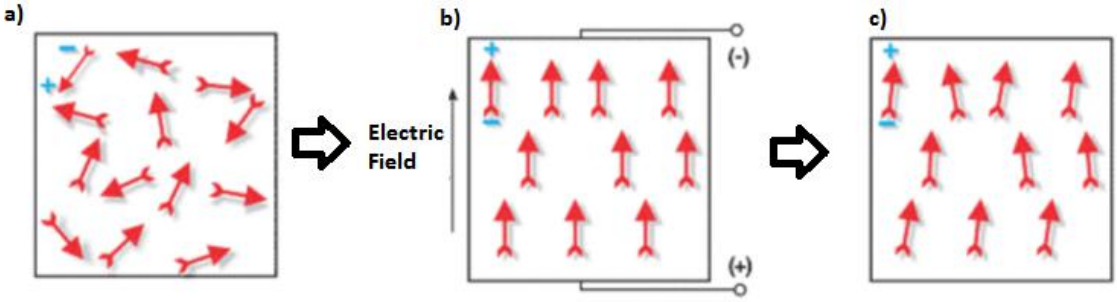

Figure 2.7: Polarizing of a piezoelectric ceramic. a) Randomly oriented dipoles. b) Aligned dipoles under strong electric field. c) Permanently elongated polarization tendency [15].

Although polycrystalline piezoelectric materials are comparably flexible with respect to single crystal piezoelectric materials, those materials are hardly applicable to biomedical applications since organs are much softer. Even if the low stiffness is able to be achieved by thin film structure, the lead components in most polycrystalline piezoelectric materials are toxic. Piezoelectric polymer materials such as polyvinylidene fluoride (PVDF) are adequate substitute materials. Although piezoelectric polymers usually have piezoelectric coefficient, those materials are used in many biomedical applications because of the call for the flexibility and biomedical stability. Furthermore, the voltage capability is much higher than other materials, which can be used as sensor switch applications where the current is less important [18]. The piezoelectricity of PVDF is dissimilar with respect to the chain phase. The α-phase has no dipole moment since dipoles are locally compensated. On the contrary, the β-phase which hydrogen atoms and fluorine atoms are parallel in longitudinal direction has significant dipole moment. The β-phase PVDF can be artificially formed through thermal and electrical

poling process. Polymer blends such as polyvinylidene fluoride-trifluoroethylene (PVDF-TrFE) or polyvinylidene fluoride-chlolofluoroethylene (PVDF-CFE) increase ratio of the β-phase among chains [19].

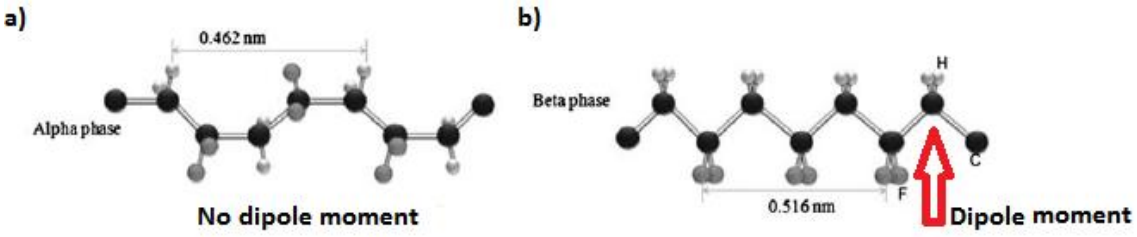

Figure 2.8: PVDF polymer chain phase. a) α-phase with no dipole and b) β-phase with dipole moment [20].

2.3 PIEZOELECTRIC ENERGY HARVESTING CIRCUIT

As the electric power output of piezoelectric energy harvesters is low and instant, the storage circuit is desired. The generated output by the energy harvester is basically AC output. To conserve the energy, the output should be DC; therefore, the full bridge rectifier is required to unify the sign of the AC output. Then, the rectified output is stored into the capacitor; the energy stored in the capacitor can be used as a DC source later. The Figure 2.9 and the Figure 2.10 describe a simple design of the piezoelectric energy harvesting circuit and its output signal, respectively[21].

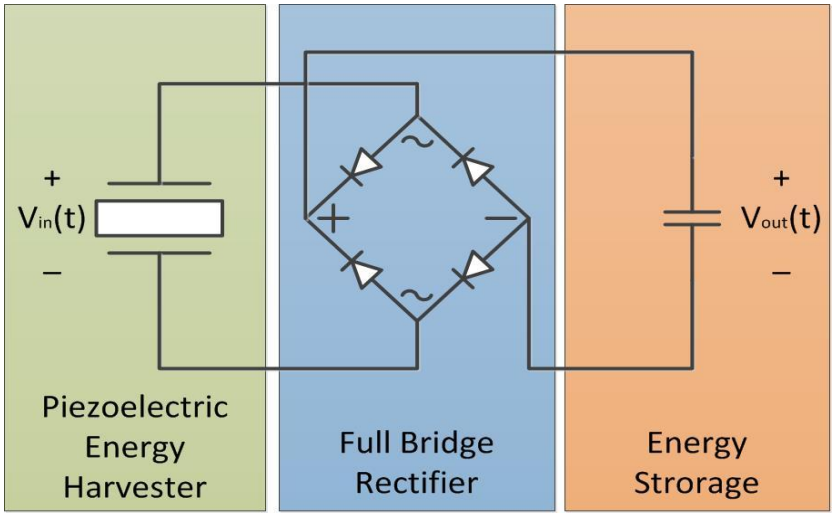

Figure 2.9. A design of the piezoelectric energy harvesting circuit.

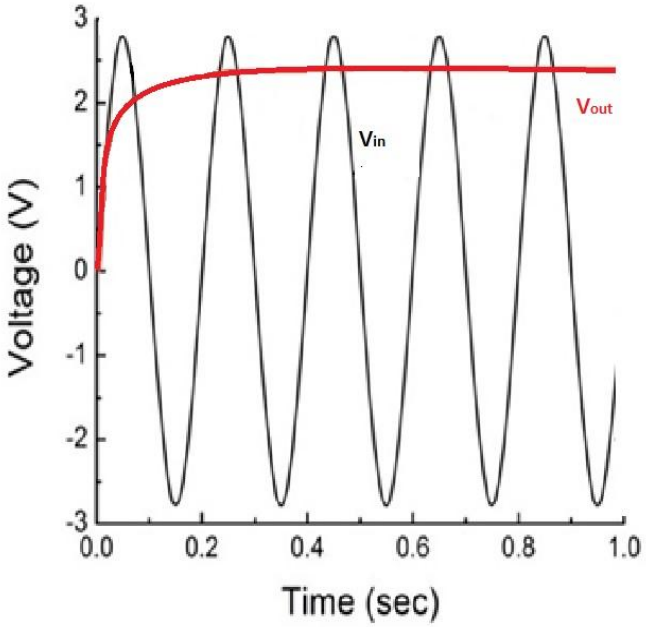

Figure 2.10. The electric output signal of the piezoelectric energy harvesting circuit.

Chapter 3 : Thickness Optimization of Flexible PVDF-TrFE Unimorph for Biomedical Energy Harvesting

A blanket structure is the lamination of a blanket piezoelectric layer on a blanket flexible polymer substrate; for example PVDF-TrFE on Kapton. When the unimorph bends, the piezoelectric PVDF layer deforms and generates electrical power. The voltage and power output depends on the thickness of the PVDF but the relation might not be monotonic. Therefore the goal of this chapter is to establish a deterministic electromechanical model for the PVDF unimorph where the relation between. First the mechanical analysis of the structure is covered, focusing on the stress derivation in the pure bending condition. Then the polarization induced from the stress derived from the previous section is analyzed, which eventually forms the charge. Using general electrostatic theory, the voltage, charge and electric energy are derived. Next two sections cover the thickness optimization under the moment controlled condition and curvature controlled condition. Both sections are under the pure bending condition. Fifth section shows the feasibility of the pure bending condition by comparing it to the practical load condition. The cantilever bending is a very practical and common bending condition with the real load. In this case, uniform loading on the top surface is given. Last section depicts the effect of the Young's modulus ratio on the thickness optimization.

3.1 Mechanical Analysis

Piezoelectric polarization is derived from stress distribution in a piezoelectric material. The stress analysis in a structure, therefore, is essential to estimate final electric

output. Since our device will be attached to the epicardiac surface, which is relatively soft compared to the structure, the situation can be simplified to the classical beam bending theory. The classical beam bending theory, also known as the Euler-Bernoulli beam theory, describes a relationship between the deflection of a beam and the applied load to the beam[22].

$$\nabla^2\nabla^2 w = \frac{q}{Y \cdot I} \tag{3.1}$$

The Equation (3.1) is called Euler-Bernoulli Equation, where *w* is the neutral surface deflection vector of the structure in z direction, q is the load applied and $Y \cdot I$ is the flexural rigidity of the structure. From this equation, we can find the curvature of the beam bending and then find the longitudinal strain distribution in the structure. Once the longitudinal strain distribution is defined, the longitudinal stress distribution also can be described easily. Since pure bending condition postulates no load is applied to the structure, the load term q becomes zero. Then assuming the solution of the Equation (3.1) is polynomial, the deflection vetor *w* becomes

$$w = A_1 + A_2 x + A_3 x^2 + A_4 x^3 \tag{3.2}$$

where A_i is the coefficient of each term. The variable *x* is the longitudinal direction of the beam structure. Now we have to define each coefficient with boundary condition. The moment is defined as

$$M = -YI\left(\frac{\partial^2 w}{\partial x^2}\right) \tag{3.3}$$

If we consider the moment is uniform in longitudinal direction over the structure, we can apply the following boundary condition

$$x = \pm\frac{L}{2},\ M = M_0 \tag{3.4}$$

where L is the length of the structure and M is the moment, so that A_4 becomes zero. We also assume that there is no displacement in transverse direction (z-direction) at the middle of the structure

$$x = 0,\ w = \frac{\partial w}{\partial x} = 0 \tag{3.5}$$

so that A_1 and A_2 becomes zero. Thus, the deflection vector w becomes

$$w = -\frac{M_0}{2YI}x^2 \tag{3.6}$$

The negative sign means the bending is downward. Now the curvature of the beam can be calculated considering the slope of a beam in x-axis direction, which can be described as

$$\theta(x) = \frac{dw}{dx} \tag{3.7}$$

where θ is the bending angle of the neutral surface. Since the length of infinitesimal x component is the product of radius and the angle, the curvature, which is the reciprocal of the radius, can be written as

$$\kappa = \frac{1}{r_x} = \frac{d\theta}{dx} = \frac{d^2w}{dx^2} \tag{3.8}$$

where κ represents the curvature and r_x is the radius of the bending. From the Equation (3.6) and (3.8) the curvature can be rewritten as

$$\kappa = \frac{M_0}{YI} \tag{3.9}$$

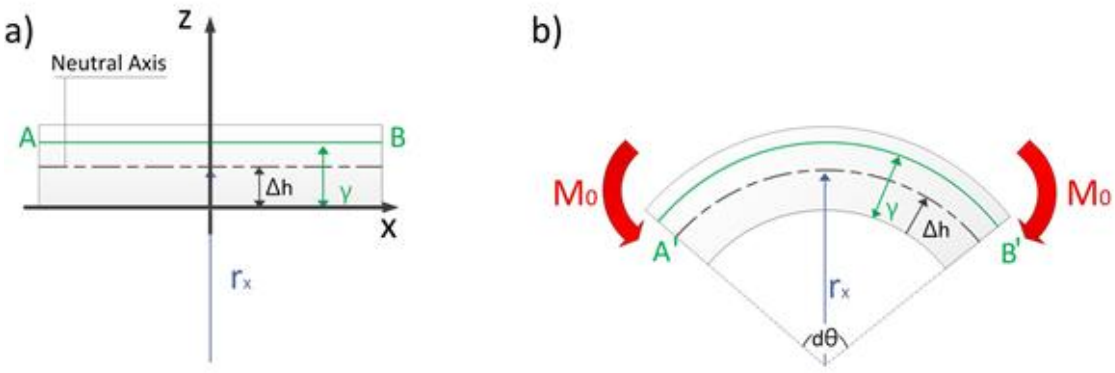

Figure 3.1: Simple bending schematics. a) Simple beam structure schematic before bending. b) Moment applied simple beam structure bending.

The simple bending is described in Figure 3.1 above. For the derivation of the strain, let us consider a segment at a distance γ from the bottom of the beam structure. For convenience sake, γ is defined as a new z-directional coordinate, assuming the x axis exists at the bottom surface of the structure. As depicted, the length before bending is $\overline{AB}$ while the length after bending is $\overline{A'B'}$. Assuming the angle between A' and B' is infinitesimal; we can express the length $\overline{AB}$ and $\overline{A'B'}$ as $\overline{AB} = r_x \cdot d\theta$ and $\overline{A'B'} = (r_x + (\gamma - \Delta h)) \cdot d\theta$, where Δh is the z-direction distance between the neutral surface and the bottom surface of the beam when x-axis lies on the bottom surface of the beam. The neutral surface, or the neutral axis, is the longitudinal cross section of a beam where longitudinal strain or stress becomes zero. The neutral axis lies on the geometric

centroid if the structure is ideally symmetric and isotropic [23]. The longitudinal strain S_1, which is defined as the ratio of deformation, thereby, can be expressed as

$$S_1 = \frac{\overline{A'B'} - \overline{AB}}{\overline{AB}} = \frac{\gamma - \Delta h}{r_x} = (\gamma - \Delta h_1)\kappa \qquad (3.10)$$

The Equations from (3.1) to (3.10) are for a beam composed of a single material. In our application, however, is a blanket structure as can be seen in Figure 3.2 below. For the detailed analysis, a longitudinal section of the structure will be used, as described in the Figure 3.3.

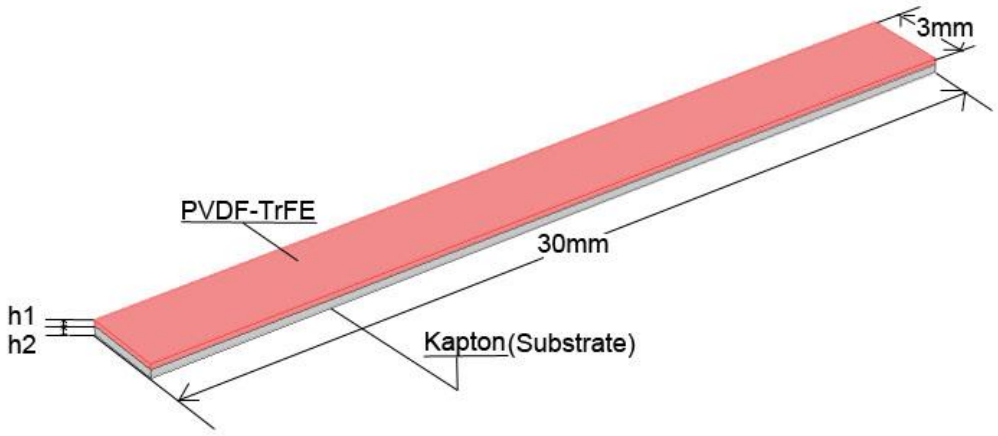

Figure 3.2: Blanket structure schematics.

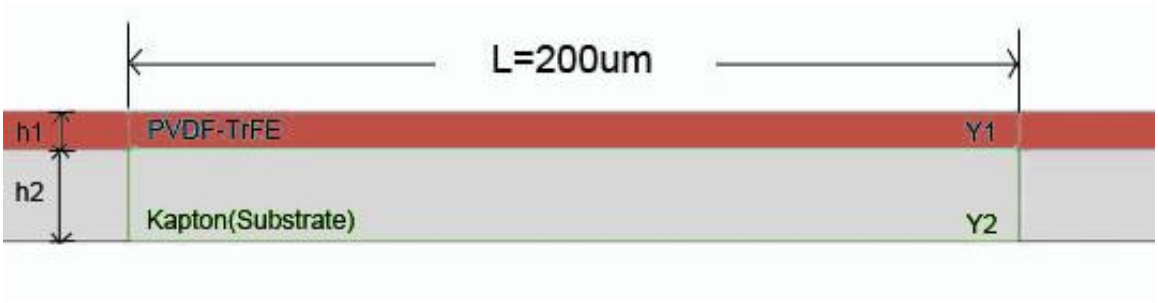

Figure 3.3: A longitudinal section of the blanket structure.

To analyze the blanket structure in terms of the classical beam theory, first we have to calculate the z-direction position of the neutral axis of the structure. As mentioned above, the neutral axis lies on the geometric centroid if the structure is geometrically and materially symmetric and isotropic. In the blanket structure, on the other hand, the position of the neutral axis depends on the ratio of the thickness and Young's modulus between two materials.

Assuming the two layers share the same value of Poisson's ratio, the neutral axis of the bilayer laminate is given by

$$\Delta = \frac{1+2\Sigma\eta+\Sigma\eta^2}{2\eta(1+\Sigma\eta)},\ \Delta h_1 = \textit{Neural Axis} \qquad (3.11)$$

where $\eta = h_1 / h_2$ is the thickness ratio, $\Sigma = \overline{Y}_1 / \overline{Y}_2$ is the modulus ratio, and $\overline{Y}_n = Y_n(1-\nu^2),\ n=1,2$ [24] is the plane strain modulus. $\overline{Y}$ is derived from the plane stress condition where ν is the Poisson's ratio and Y is the material's Young's modulus. In our case, we can use the plane stress condition since z-direction stress in the thin film structure is ignorable, which postulation is called Kirchhoff's hypothesis [25]. Also, for

2D analysis on xz plane, we can assume y-direction strain S_2 is negligible, which is the plane strain condition[26]. Therefore, the postulated conditions to this blanket structure are the plane stress condition in z direction and the plane strain condition in y direction. Originally, the stress-strain compliance matrix and stiffness matrix for an isotropic material are given by

$$\begin{bmatrix} S_1 \\ S_2 \\ S_3 \\ S_4 \\ S_5 \\ S_6 \end{bmatrix} = \frac{1}{Y} \begin{bmatrix} 1 & -\nu & -\nu & 0 & 0 & 0 \\ -\nu & 1 & -\nu & 0 & 0 & 0 \\ -\nu & -\nu & 1 & 0 & 0 & 0 \\ 0 & 0 & 0 & 2(1+\nu) & 0 & 0 \\ 0 & 0 & 0 & 0 & 2(1+\nu) & 0 \\ 0 & 0 & 0 & 0 & 0 & 2(1+\nu) \end{bmatrix} \begin{bmatrix} T_1 \\ T_2 \\ T_3 \\ T_4 \\ T_5 \\ T_6 \end{bmatrix} \tag{3.12}$$

$$\begin{bmatrix} T_1 \\ T_2 \\ T_3 \\ T_4 \\ T_5 \\ T_6 \end{bmatrix} = Y \begin{bmatrix} 1-\nu & \nu & \nu & 0 & 0 & 0 \\ \nu & 1-\nu & \nu & 0 & 0 & 0 \\ \nu & \nu & 1-\nu & 0 & 0 & 0 \\ 0 & 0 & 0 & \frac{(1-2\nu)}{2} & 0 & 0 \\ 0 & 0 & 0 & 0 & \frac{(1-2\nu)}{2} & 0 \\ 0 & 0 & 0 & 0 & 0 & \frac{(1-2\nu)}{2} \end{bmatrix} \begin{bmatrix} S_1 \\ S_2 \\ S_3 \\ S_4 \\ S_5 \\ S_6 \end{bmatrix} \tag{3.13}$$

where $Y = Y/(1+\nu)(1-2\nu)$, T is the stress and S is the strain. In our case, as mentioned above, xz plane is the only plane we are interested, thereby, S_2 is considered to be negligible, including y-direction related shear strains S_4 *and* S_6. Consequently, the stress components y-direction included can be also negligible. Then the simplified 2D stiffness matrix and the compliance matrix become

$$\begin{bmatrix} T_1 \\ T_3 \\ T_5 \end{bmatrix} = \begin{bmatrix} (1-\nu)Y & \nu Y & 0 \\ \nu Y & (1-\nu)Y & 0 \\ 0 & 0 & G \end{bmatrix} \begin{bmatrix} S_1 \\ S_3 \\ S_5 \end{bmatrix} \tag{3.14}$$

$$\begin{bmatrix} S_1 \\ S_3 \\ S_5 \end{bmatrix} = \begin{bmatrix} \frac{(1-\nu^2)}{Y} & -\frac{\nu(1+\nu)}{Y} & 0 \\ -\frac{\nu(1+\nu)}{Y} & \frac{(1-\nu^2)}{Y} & 0 \\ 0 & 0 & \frac{1}{G} \end{bmatrix} \begin{bmatrix} T_1 \\ T_3 \\ T_5 \end{bmatrix} \tag{3.15}$$

where $G = Y / 2(1+\nu)$ [26]. Herein, z direction stress is zero with the thin film postulation given above. In addition, for pure bending case, the shear strain S_5 and the shear stress T_5 is negligible [25]. Furthermore, these shear strain and stress are dimensionally irrelevant to the piezoelectric coupling coefficient in this case [27]. Therefore, the remained longitudinal x-direction stress T_1 can be expressed with two strain terms, S_1 and S_3, and vice versa.

$$T_1 = (1-\nu)YS_1 + \nu YS_3 \tag{3.16}$$

$$S_1 = \frac{(1-\nu^2)}{Y} T_1 \tag{3.17}$$

$$S_3 = -\frac{\nu(1+\nu)}{Y} T_1 \tag{3.18}$$

Arranging Equations (3.16) to (3.18) in terms of S_1 and substituting (3.10) to S_1, the longitudinal stress T_1 can be expressed in γ,

$$T_{1n} = (\gamma - \Delta h_1)\bar{Y}_n \kappa, \ \ n = 1, 2 \tag{3.19}$$

where *n* represents the materials; 1 is PVDF-TrFE and 2 is Kapton substrate. If the range of γ is $h_2 < \gamma < h_1 + h_2$, then n is intuitively 1. The Equation (3.19) shows that the stress above the neutral axis is positive while the stress below the neutral axis is negative. In mechanics, the positive stress means tension whereas the negative stress means compression [22]. Furthermore, the magnitude of the stress varies with respect to the transverse distance between an arbitrary point and the neutral axis. The further the arbitrary point locates from the neutral axis, the larger the magnitude of the stress becomes. The Figure 3.4 below depicts the Equation (3.19).

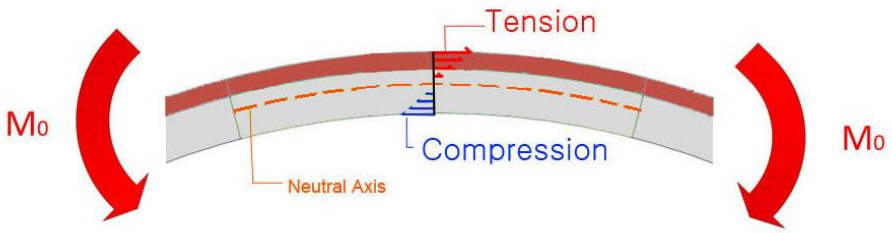

Figure 3.4: The stress distribution of the blanket structure.

The term $\bar{Y}_n$ explains that the stress distribution may be changed within different materials, while the strain is continuous regardless of the material [22]. In our case, for example, the increment of the stress in PVDF-TrFE will be larger than that of the stress in Kapton. In COMSOL simulation, the stress gap at the boundary of two materials and the slope difference in two different material regions reflect the relation between the Young's modulus and the stress, as seen in the Figure 3.5 below.

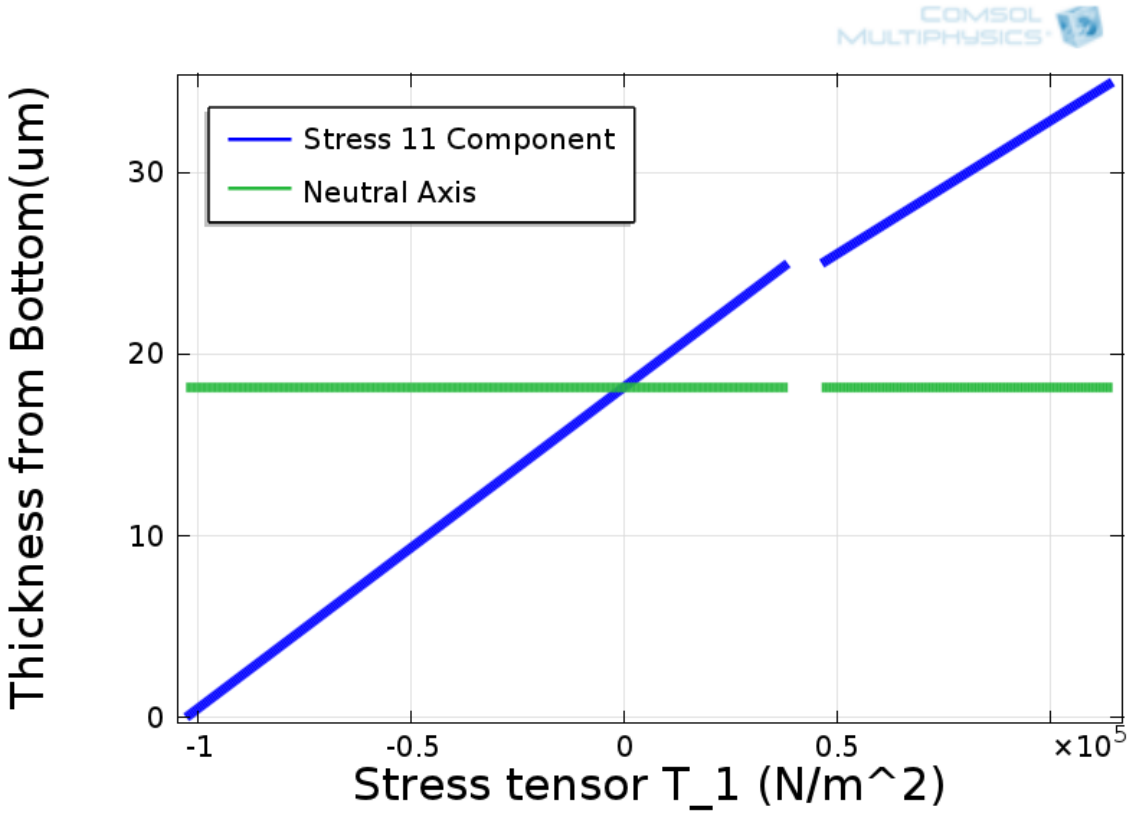

Figure 3.5: Longitudinal stress distribution and the neutral axis location within the blanket structure. (PVDF-TrFE thickness = 10um)

The Figure 3.6 shows the simulation result of the longitudinal and transverse stress. The stress tensor in transverse direction is relatively negligible compared to the stress tensor in longitudinal direction, which is obvious that the simulation follows the thin film postulation. The magnitude of the tensional maximum stress at PVDF-TrFE is slightly larger than that of the compressional maximum stress at Kapton, as expected.

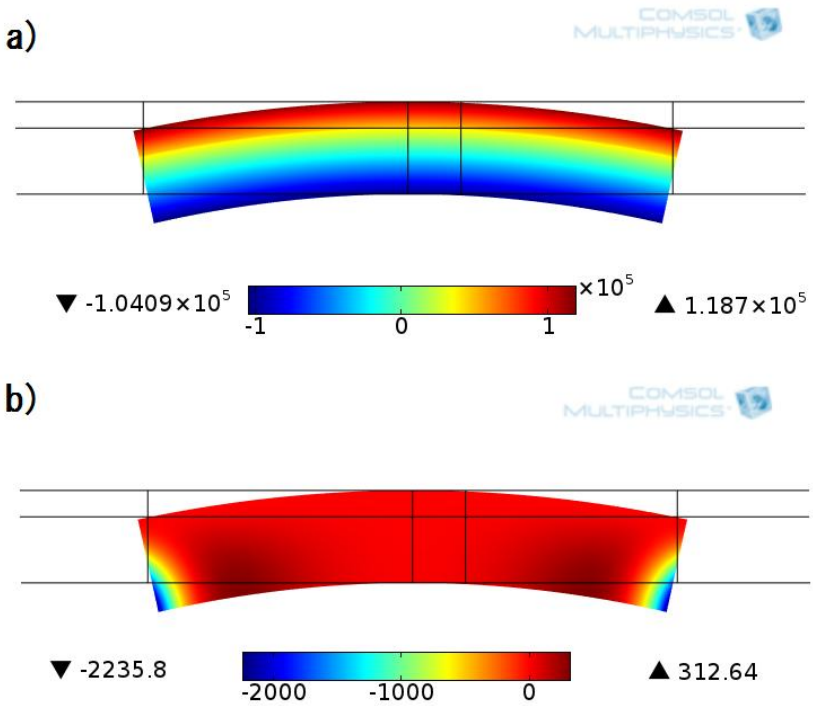

Figure 3.6: COMSOL simulation stress distribution a) stress tensor x-x direction (T_1) and b) stress tensor z-z direction (T_3). (PVDF-TrFE thickness=10um)

The ratio between S_1 and S_3 can be derived by substituting the Equation (3.19) into (3.17) and (3.18).

$$S_3 = -\frac{\nu}{(1-\nu)} S_1 \tag{3.20}$$

This relation can be observed in the simulation result, as described in the Figure 3.7 below. Assuming the Poisson's ratio of both materials is equal to 0.34[28, 29], the theoretical ratio between the stress tensors is -0.515. In the simulation results, the ratio of the maximum tension or compression strain between two different tensors is also almost

-0.515, which shows that the simulation result is well matched to the theoretical computation.

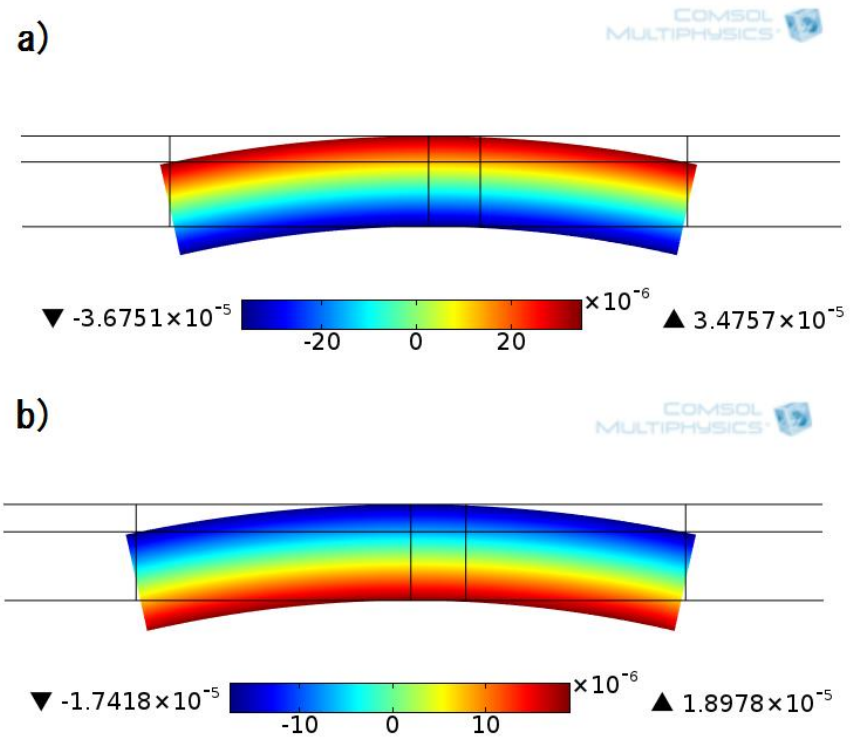

Figure 3.7: Simulation strain distribution a) strain tensor x-x direction (S_1) and b) strain tensor z-z direction (S_3). (PVDF-TrFE thickness=10um)

The curvature term κ in the Equation (3.19) denotes that the stress is manipulated by the curvature. In usual situation, it is true that the variation of the curvature could induce the longitudinal stress in bending. For instance, the output of an energy harvesting device attached to a wrist may depend on the degree of the curvature, regardless of the device structure parameter. In other words, wrist can generate any dependent force or moment to achieve the desired curvature, if the material stiffness of

the device is reasonable. This statement can be clearly explained with the Equation (3.9). When the curvature term κ at the left is fixed, the moment term *M* at the right will be changed with different structures since the structure property term, flexural rigidity *YI*, varies. In our application, however, the curvature – moment relation should be reconsidered. Unlike the wrist, the human heart or lung is not controlled by the curvature but the moment since the mechanical energy generated by those organs are usually limited. In this reason, it is reasonable to assume that the moment is constant regardless of the device structure parameter. In this case, the curvature term in the Equation (3.9) changes with different structures while the moment term is constant. Then the Equation (3.19) becomes

$$T_{1n} = (\gamma - \Delta h_1)\frac{\overline{Y}_n}{\overline{Y}_2}\frac{M_0}{I}, \quad n = 1, 2 \tag{3.21}$$

The *Y* in the Equation (3.9) becomes $\overline{Y}_2$ with the plane stress assumption that transverse stress is negligible. For convenience, the Young's modulus of the substrate is set as a standard for the flexural rigidity and the second moment of inertia, as described in the Figure 3.8.

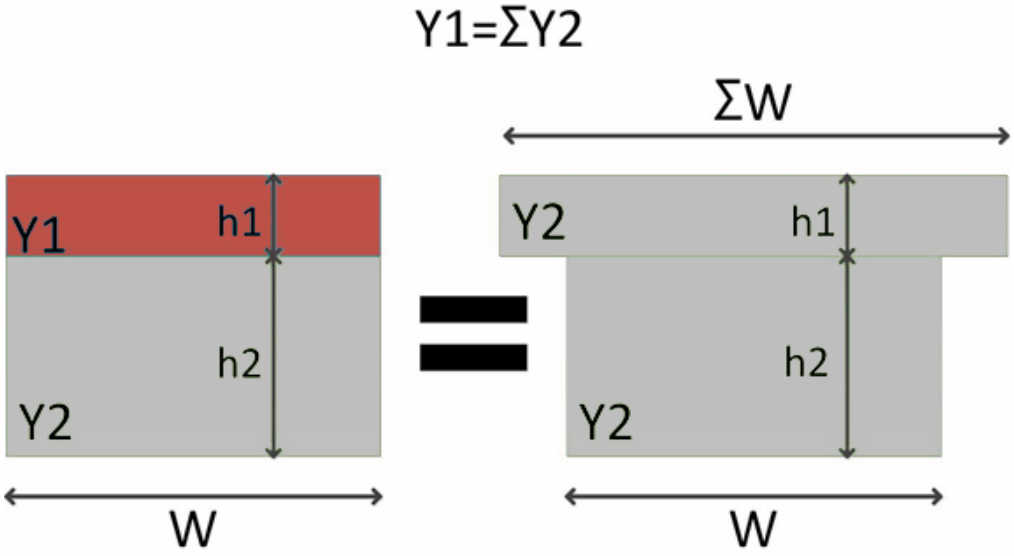

Figure 3.8: The postulation behind the second moment of inertia calculation of the blanket structure.

To calculate the second moment of inertia, the equivalent area method is applied [30]. The equivalent area method enables the analysis of a composite beam of which the cross section is rectangular as a single material beam of which the cross section is T-shaped.

Using this method, the second moment of inertia I of the blanket structure for the cross-section on y-z plane, is given as

$$I = W\left\{\Sigma\frac{h_1^3}{12} + \Sigma h_1\left(\frac{h_1}{2} + h_2 - \Delta h_1\right)^2 + \frac{h_2^3}{12} + h_2\left(\Delta h_1 - \frac{h_2}{2}\right)^2\right\} \qquad (3.22)$$

where W is the width of the structure[30].

Now we have to establish an arbitrary constant moment generated by a human heart. Considering the human heart as a sphere, the average radius of the human heart is

approximately 5cm [31]. The radius changes with respect to the cardiac cycle. The cardiac cycle has two periods; the period refilling blood is called systole whereas the period relaxing and preparing next systole is called diastole [32]. Intuitively, the radius is maximum during the diastole and minimum during the systole. Based on a study which has the data of epicardiac transverse strain, the average maximum and minimum strain is approximately 5%, as described in Figure 3.9 a) [33]. Using this information with our structure parameters, the angular displacement and eventually, the moment can be calculated.

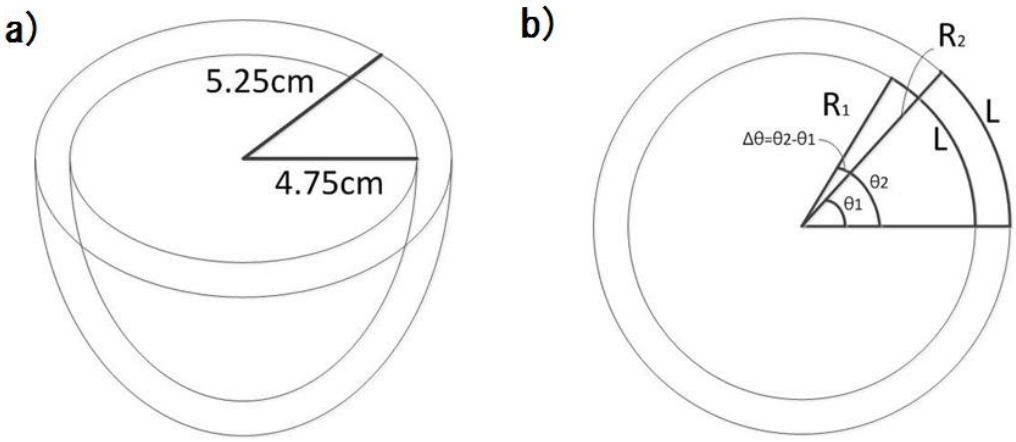

Figure 3.9: a) Simple geometric epicardiac model. 5.25cm for the maximum radius at diastole and 4.75cm for the minimum radius at systole. b) Transverse section analysis of the epicardiac strain.

From the Figure 3.2, the structure length L is given as 30mm. The angular difference $\Delta\theta = L/\mathrm{R}_1 - L/R_2$ in the Figure 3.11 b) is about 0.0602 [rad]. Then the calculated curvature of the bending is $1/r_x = \Delta\theta/L = 2\ m^{-1}$. However, the curvature will

be changed when the thickness of the film varies, since the second moment of inertia will be also changed. Therefore, establishing an arbitrary standard thickness is required, which is 10um PVDF-TrFE and 25um Kapton in this case. With given parameters and the Equation (3.22), the second moment of inertia is $1.1656\times10^{-17}\ m^4$. The consequent moment from the Equation (3.9) is $M_0 = 6.5895\times10^{-8}\ N\cdot m$. This moment value will be used as a constant moment for all structures from now on.

3.2 PIEZO-ELECTROSTATIC ANALYSIS

First let us consider the basic piezoelectric Equation (2.4) from chapter 2. Since there is no external electric field, the electric displacement field generated by the stress can be written as

$$D_3 = d_{31}T_1 = P_3 \tag{3.23}$$

where $h_2 < \gamma < h_1 + h_2$ [34]. The polarization term P_3 is stress-induced spontaneous polarization and the subscript 3 indicates the film thickness direction. As can be seen, the piezoelectric coefficient now represents the specific mode in terms of the stress-electric displacement field interaction direction. As mentioned, there is no internal electric field but the stress-induced polarization at the quasi-static moment; $E_3 = 0,\ P_3 = d_{31}T_1$. Thus, the Equation (3.23) is acceptable expression. To emphasize the stress-induced polarization, P_3 will be used as the notation instead of D_3. By substituting (3.21) to (3.23), the Equation (3.23) can be rewritten as

$$P_3 = d_{31}(\gamma - \Delta h_1)\Sigma \frac{M_0}{I} \qquad (3.24)$$

where $h_2 < \gamma < h_1 + h_2$. The Equation (3.24) indicates that the stress-induced polarization varies in terms of the transverse location, which is reasonable regarding the stress distribution under the pure bending condition. The polarization distribution is depicted in the Figure 3.10 a). Here we assume that the film was poling-processed by the bottom-up electric field. The polarization vector direction, which is from a negative charge to a positive charge as shown in the Figure 3.10 b), depends on the sign of stress and the coupling coefficient, which is positive in PVDF-TrFE case. Therefore, the polarization is upward in the tension region, while it is downward in compression region.

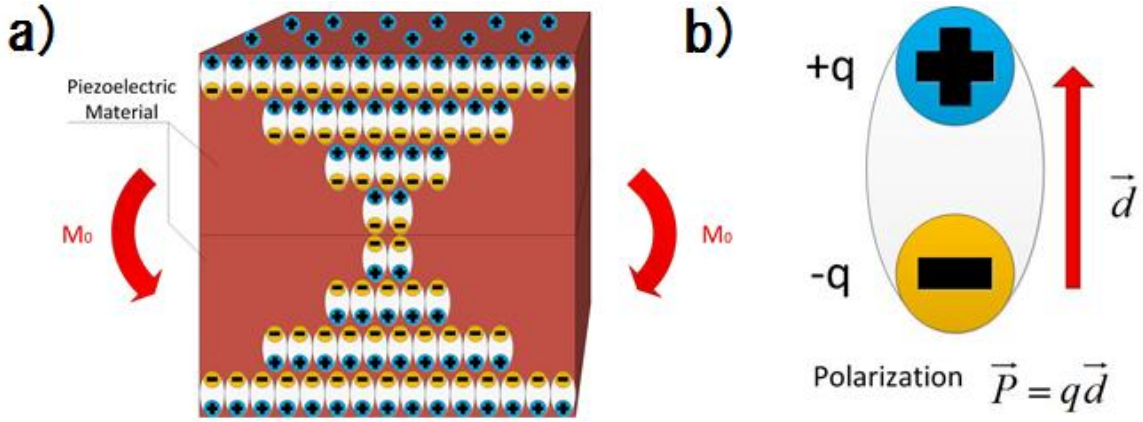

Figure 3.10: a) The polarization distribution of a piezoelectric generator under the pure bending condition and b) polarization direction.

The polarization direction is crucial to piezoelectric applications under bending condition. If electrodes are connected to the top and bottom of the structure in the Figure

3.10 a), no voltage will be generated since their electric potential is equivalent. There are two methods to solve this problem; 1) using a substrate material for the compressional or tensional region and 2) manipulating polarization direction by separate poling process or insertion of an electrode at the centroid surface [35]. Former method consequently will be a unimorph structure, while the latter method will be a bimorph structure, which is relatively efficient. For our application, however, a relevant insulator substrate is required since attaching an electrode material to the epicardiac surface directly is not feasible.

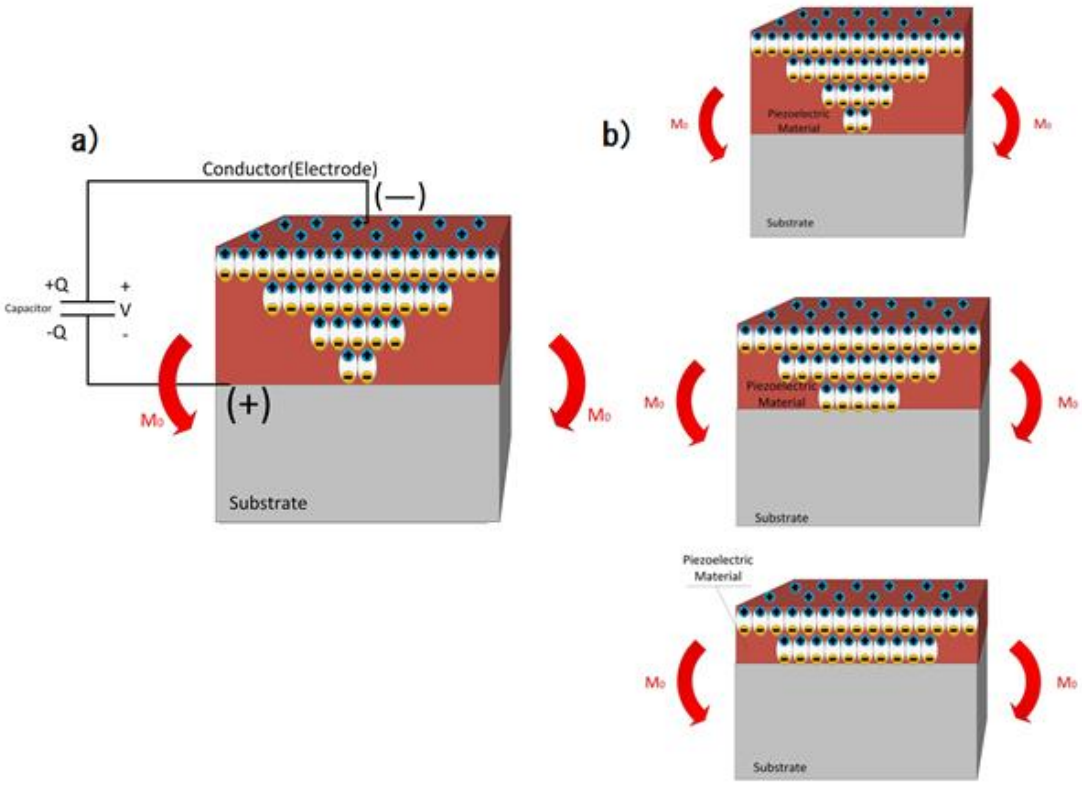

Figure 3.11: a) The polarization distribution and the electric output of a bending unimorph piezoelectric generator. b) The polarization distribution with respect to the thickness variation.

Under the unimorph bending condition shown in the Figure 3.11 a), geometric parameters such as the top surface area and the thickness ratio of the piezoelectric material and the substrate material apparently affect the electric output. In our application, the area applied to the epicardiac surface will be limited while the film thickness ratio is able to be controlled comparably. Assuming the thickness of the substrate remained as the same, varying the thickness of the piezoelectric material will change the electric output, as described in the Figure 3.11 b). This is evident with the Equation (3.24). The polarization is affected by the second moment of inertia term which contains the material thickness and the width information.

Although the polarization occurs in all volume of the piezoelectric material, the charge is only collectable over the surface. The overall volume polarization charge density is zero because polarization charges generated in the body cancel each other out [11]. The surface polarization charge density is the inner product of the polarization and the surface normal vector.

$$\mathbf{a_n} \cdot \mathbf{P} = \rho_{ps} \tag{3.25}$$

The surface normal vector of the top surface is upward (positive) whereas that of the bottom surface is downward (negative). Assuming the stress-induced polarization direction is upward by the poling process, the polarization charge density on the top and bottom surface are

$$\rho_{ps\_top} = +P_3\Big|_{\gamma=h_1+h_2} \tag{3.26}$$

$$\rho_{ps\_bottom} = -P_3\Big|_{\gamma=h_2} \tag{3.27}$$

The sign of the charge induced to the top and bottom surface electrode is the opposite of the sign of the polarization charge density on each surface. Integrating each polarization surface charge density with the opposite sign gives the charge on each surface electrode,

$$Q_{top} = -\int_S \rho_{ps\_top} ds = -L \cdot W \cdot P_3\Big|_{\gamma=h_1+h_2} \tag{3.28}$$

$$Q_{bottom} = -\int_S \rho_{ps\_bottom} ds = L \cdot W \cdot P_3\Big|_{\gamma=h_2} \tag{3.29}$$

where L is the length of the longitudinal section of the structure described in the Figure 3.3, W is the width of the structure. Substituting the Equation (3.24),

$$Q_{top} = -L \cdot W \cdot d_{31}(h_1 + h_2 - \Delta h_1)\Sigma \frac{M_0}{I} \tag{3.30}$$

$$Q_{bottom} = L \cdot W \cdot d_{31}(h_2 - \Delta h_1)\Sigma \frac{M_0}{I} \tag{3.31}$$

The Equation (3.30) and (3.31) show the amount of the charge on each surface is different. For convenience, the equivalent charge method is applied. The method postulates that each surface electrode has the charge of which the amount is equivalent but the pole is opposite, while the total amount of the generated charge remains equal. Using this method enables the model to be regarded as a parallel plate capacitor, assuming no electric flux loss through side surfaces.

$$Q_{generated} = \left|Q_{top}\right| + \left|Q_{bottom}\right| = LW \cdot d_{31}(h_1 + 2h_2 - 2\Delta h_1) \cdot \Sigma \frac{M_0}{I} \tag{3.32}$$

$$Q_{equivalent} = \frac{Q_{generated}}{2} = LW \cdot d_{31} \frac{(h_1 + 2h_2 - 2\Delta h_1)}{2} \cdot \Sigma \frac{M_0}{I} \qquad (3.33)$$

The capacitance depends on the structure and the permittivity. In our case, the structure is equivalent to the parallel plate capacitor of which the capacitance is $C = \varepsilon_p LW / h_1$. Using the relation between the voltage, capacitance and charge, often denoted as $Q=CV$, the voltage is achievable.

$$V = \frac{Q_{equivalent}}{C} = h_1 \frac{d_{31}}{\varepsilon_p} \frac{(h_1 + 2h_2 - 2\Delta h_1)}{2} \cdot \Sigma \frac{M_0}{I} \qquad (3.34)$$

However, the real electric field cannot be obtained with the equivalent charge method. To derive the electric field, another derivation approach is required. From the Equation (3.23), the polarization can be regarded as an external electric field [34]. Especially in our case, there is no electric field but the polarization at the quasi-static moment. Assuming imaginary charges outside which has the equivalent electric energy to the generated polarization, the equivalent external electric field generated by the imaginary charges in the piezoelectric material is

$$E_3 = \frac{P_3}{\varepsilon_p} = \frac{d_{31}}{\varepsilon_p} (\gamma - \Delta h_1) \Sigma \frac{M_0}{I} \qquad (3.35)$$

where $h_2 < \gamma < h_1 + h_2$. The electric field vector direction is equivalent to the polarization, which is bottom-up. Since the relation between the electric field and electric potential is $\mathbf{E} = -\nabla V$, the voltage derived from the Equation (3.35) is

$$V = -\int_{h_1+h_2}^{h_2} \mathbf{E}_\gamma \, d\boldsymbol{\gamma} = h_1 \cdot \frac{d_{31}}{\varepsilon_p} \frac{h_1 + 2h_2 - 2\Delta h_1}{2} \cdot \Sigma \frac{M_0}{I} \qquad (3.36)$$

which is equivalent to the Equation (3.34). Therefore, the equivalent charge method is reasonable. For the dimensionless notation, the Equation (3.33) and (3.34) can be rewritten as

$$Q_{eqv} = LWh_2 \cdot d_{31}\left(1+\frac{\eta}{2}-\Delta\eta\right)\cdot\Sigma\frac{M_0}{I} \tag{3.37}$$

$$V = h_1 h_2 \cdot g_{31}\left(1+\frac{\eta}{2}-\Delta\eta\right)\cdot\Sigma\frac{M_0}{I} \tag{3.38}$$

where $g_{31} = d_{31} / \varepsilon_p$. As described in the Equation (3.38), the voltage output is not affected by the surface area, except the width term in the second moment of inertia. Beware that charge expression in (3.37) is not the real value; the real charge value in each electrode is in (3.30) and (3.31).

3.3 THICKNESS OPTIMIZATION UNDER CONSTANT MOMENT

As mentioned a couple of times, the only feasibly controllable parameter is the thickness of the piezoelectric material and the substrate. The length and width of the device is hard to be manipulated because of the dimensional limitation of the organs [31]. Other material parameters, such as the Young's modulus ratio or the piezoelectric coefficient are decided when choosing materials and only few options are available [19]. Furthermore, the thickness of the substrate is usually fixed since the commercial product film is often used as a substrate. The thickness of the piezoelectric material, however, at least in our case, can be manipulated by the spin coating process. The piezoelectric

polymer such as PVDF-TrFE is soluble into certain solutions and can be spin-coated over the substrate [36]. By controlling the solution amount, the ratio of the materials, the speed of the rotation and the exposure time, the desired thickness is able to be acquired. Therefore, investigating the effect of the piezoelectric material thickness variation before the real experiment is meaningful work to our application. Thickness optimization simulation using COMSOL was done by M. Guizzetti [37]. However, the theoretical approach and the effect of the Young's modulus were not depicted well. Also, the load and boundary condition is not applicable to our situation. Thereby, new simulation work is required.

The geometric parameters described in the Figure 3-3 are used in the COMSOL simulation. The required elastic properties for Kapton and PVDF-TrFE are the density, the Young's modulus and Poisson's ratio, which are 1300 kg/m^3, 2.5 GPa and 0.34 for Kapton and 1879 kg/m^3, 3GPa and 0.34 for PVDF-TrFE, respectively [28, 29, 38]. These values are provided assuming the material is isotropic. For the piezoelectric analysis, the compliance tensor matrix, relative permittivity matrix and coupling tensor matrix are required [12].

-Elastic Compliance Tensor

$$s^E = \begin{bmatrix} 333 & -113.3 & -113.3 & 0 & 0 & 0 \\ -113.3 & 333 & -133.3 & 0 & 0 & 0 \\ -113.3 & -113.3 & 333 & 0 & 0 & 0 \\ 0 & 0 & 0 & 893.2 & 0 & 0 \\ 0 & 0 & 0 & 0 & 893.2 & 0 \\ 0 & 0 & 0 & 0 & 0 & 893.2 \end{bmatrix} \times 10^{-12} Pa^{-1} \quad (3.39)$$

-Relative Permittivity Matrix

$$\varepsilon^T = \begin{bmatrix} 7.9 & 0 & 0 \\ 0 & 7.9 & 0 \\ 0 & 0 & 7.9 \end{bmatrix} \times \varepsilon_0 \quad (3.40)$$

-Piezoelectric Coupling Tensor

$$d = \begin{bmatrix} 0 & 0 & 0 & 0 & -36.3 & 0 \\ 0 & 0 & 0 & -40.6 & 0 & 0 \\ 10.7 & 10.1 & -33.5 & 0 & 0 & 0 \end{bmatrix} \times 10^{-12} C \cdot N^{-1} \quad (3.41)$$

The compliance tensor matrix directly derived from the matrix (3.12). The piezoelectric coupling matrix, however, cannot be directly applied to the simulation. Unlike the compliance matrix, the coupling matrix is asymmetric and sensitive to the dimension. Our simulation work is in 2D; COMSOL recognize 2D as x-y plane of the 3D. Although COMSOL has a function to use customized coordinates, there is a simple way to solve this problem; swapping y and z coordinates of the coupling matrix. In addition, *d32* coefficient and the shear stress coupling coefficient are negligible because of the plane strain assumption. As a result, the coupling matrix input in the simulation is

$$d = \begin{bmatrix} 0 & 0 & 0 & 0 & 0 & 0 \\ 10.7 & -33.5 & 0 & 0 & 0 & 0 \\ 0 & 0 & 0 & 0 & 0 & 0 \end{bmatrix} \times 10^{-12} C \cdot N^{-1} \qquad (3.42)$$

For the boundary conditions, the piezoelectric model is assigned to PVDF-TrFE whereas the linear elastic model is assigned to Kapton substrate. Since pure bending moment or angular displacement loading option is not applicable in COMSOL, the prescribed displacement is used as a quasi-moment boundary condition. This is a reasonable boundary condition because the displacement by pure bending is already defined in the Equation (3.6). The prescribed displacement in z direction – y direction in the simulation – is applied from the Equation (3.6) over the bottom boundary. For the precise result, the symmetry boundary condition is applied to each side of the structure. As some side effects are expected from the boundary condition because of the edge of the structure, buffer structures with the same material condition are put on each side. Of course, the symmetry boundary condition is applied to the boundary of the left end and right end of the whole structure while whole bottom boundary is influenced by the prescribed displacement boundary condition. For the electrostatic boundary condition, the top boundary is set as the ground. The boundary not mentioned is automatically set as the free boundary condition or the zero charge condition. The mapped mesh is selected for meshing with the maximum element size 0.5 um and the minimum element size 0.01 um. To investigate the effect of the thickness variation, parametric sweep condition is added to the study step, varying the thickness of PVDF-TrFE from 0.5um to 20um with 0.5um

for each step. The Figure 3-5, 3-6 and 3-7 used the same condition at 10um PVDF-TrFE thickness.

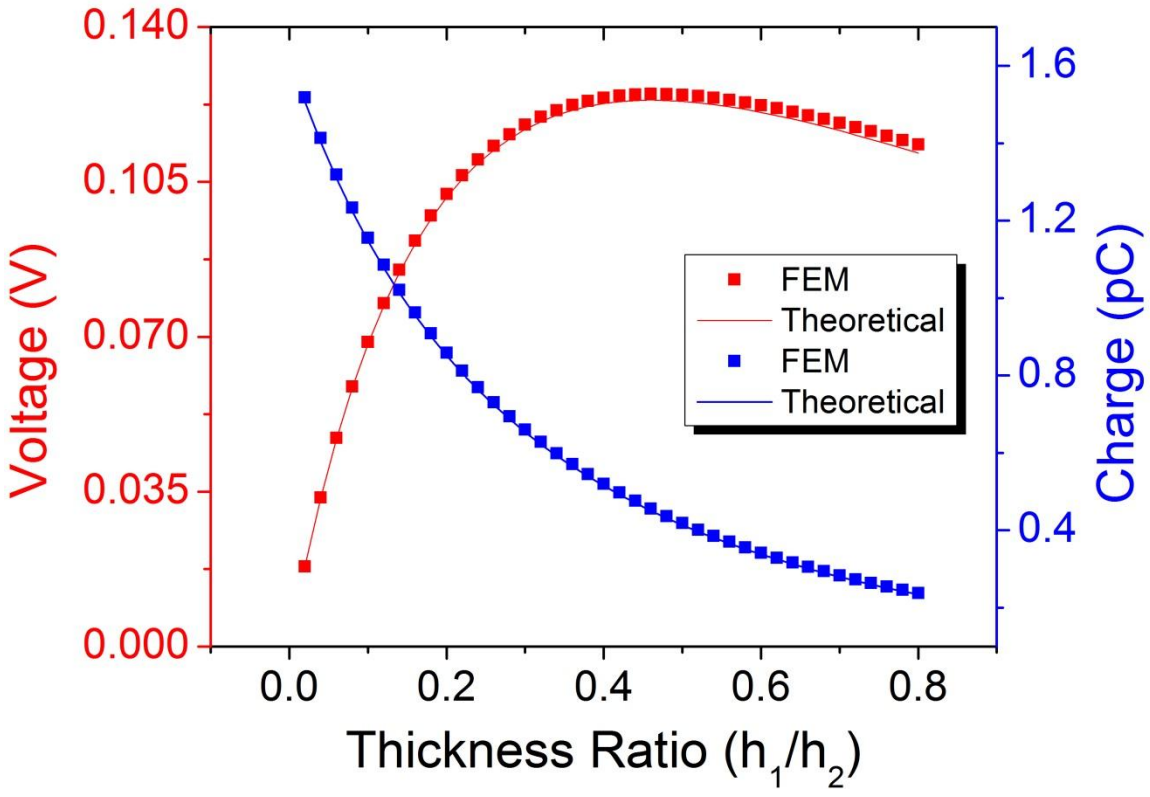

Figure 3.12: PVDF-TrFE/Kapton thickness ratio (h_1 / h_2) vs voltage (V) and charge (C) under the moment controlled pure bending condition.

Figure 3.12 shows the result of the Finite Element Method (FEM) simulation and the theoretical derivation. The voltage is collected and averaged from the bottom boundary of the effective structure which does not include the buffer structure. The charge is also collected from the same boundary. However, there is no direct simulation result for the charge; the charge is calculated from the voltage result using the Equation

(3.34). The charge density simulation given by COMSOL is related to the consequent charge from the open circuit condition, not the desired quasi-static charge. With given parameters, the voltage output shows the optimization point around the thickness ratio 0.46 with the value of 0.12488 V (0.1235 V theoretical) while the charge output shows the continuous decline. The error of the voltage output in overall step is lesser than 1.8%, which means the theory and the simulation result matches well. The error is mostly caused by two reasons; 1) the polarization generated by the coupling coefficient d_{33} and z-direction stress 2) the prescribed displacement applied to the bottom instead of the neutral axis. These errors can be reasonably neglected by the thin film postulation, unless the thickness is comparable to other geometric parameters. To optimize the structure and the electric output, however, the total electric energy should be considered.

$$Energy\ Density = \frac{1}{2}QV \tag{3.43}$$

The Figure 3.13 below shows the result of the simulation and the theoretical computation. The overall error was lesser than 3.3%, which is acceptable to insist the theoretical derivation is well matched to the simulation result. From the result, the optimized thickness ratio for the given structure is 0.18 with the energy value of 4353 pJ(4424 pJ theoretical); when the thickness of the Kapton substrate is 25um, the optimized thickness of the PVDF-TrFE should be 4.5um.

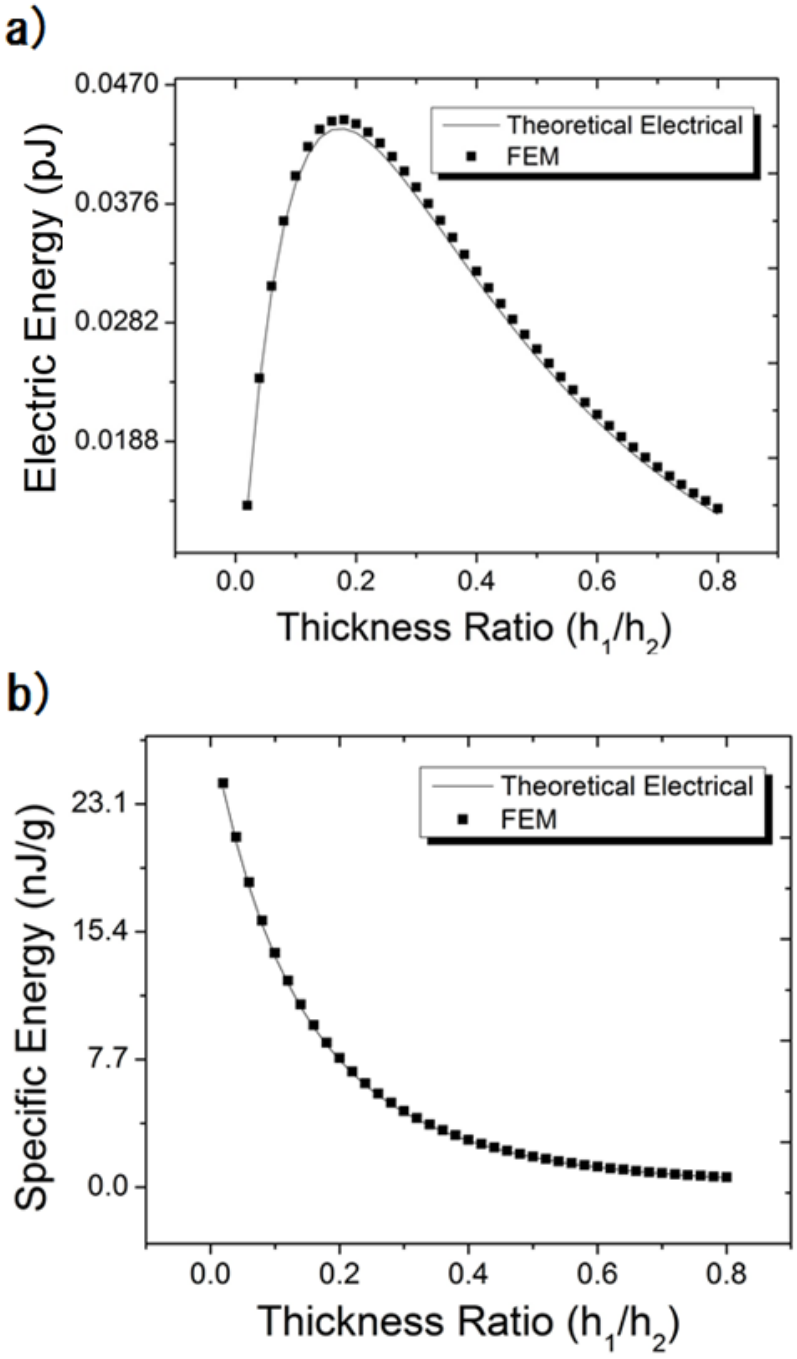

Figure 3.13: a) PVDF-TrFE/Kapton thickness ratio(h_1 / h_2) vs electric energy(J) and b) PVDF-TrFE/Kapton thickness ratio (h_1 / h_2) vs specific electric energy(J/g) under the moment controlled pure bending condition.

3.4 CONSTANT CURVATURE CONDITION

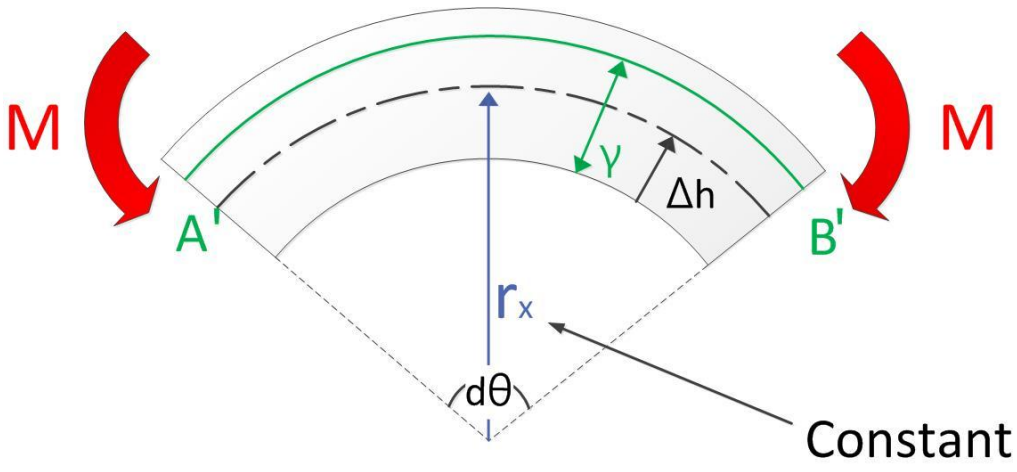

Figure 3.14: A constant curvature bending schematic.

For the broad application in future, the constant curvature condition from the Equation (3.19) is also considered. A basic curvature-controlled concept is described in the Figure 3-14. Under the constant curvature condition regarding (3.19), the Equation (3.37) and (3.38) becomes

$$Q_{eqv} = LWh_2 \cdot d_{31}\left(1+\frac{\eta}{2}-\Delta\eta\right)\cdot\overline{Y}_1\kappa \tag{3.44}$$

$$V = h_1h_2 \cdot g_{31}\left(1+\frac{\eta}{2}-\Delta\eta\right)\cdot\overline{Y}_1\kappa \tag{3.45}$$

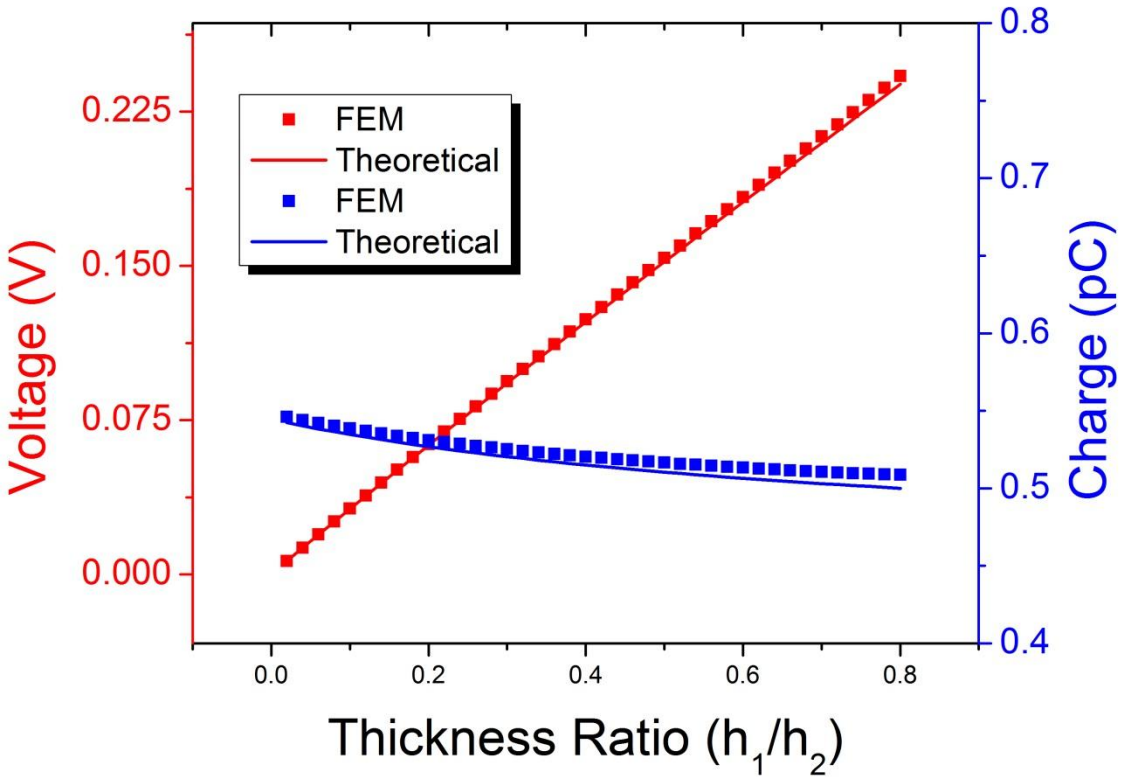

Figure 3.15: PVDF-TrFE/Kapton thickness ratio (h_1 / h_2) vs voltage (V) and charge (C) under the curvature controlled pure bending condition.

The Figure 3.15 shows the simulation result of the electric output in terms of the constant curvature condition bending. The error of the voltage output in overall step is lesser than 1.7%. In this case, the error from the coupling coefficient and z-direction stress becomes significant with increasing thickness of PVDF-TrFE, compared to the constant moment case. Still, the result is fairly acceptable. Contrary to the constant moment condition, the voltage output keeps increasing while the charge output remains almost the same. The main difference between the constant moment condition and the

constant curvature condition is the moment-second moment of inertia ratio. In the constant moment condition, the cube of PVDF-TrFE thickness term in the second moment of inertia directly affects the voltage and charge output. The constant curvature condition, in contrary, the second moment of inertia is cancelled by the varied moment to maintain the curvature constant. Therefore, the PVDF-TrFE thickness term in the Equation (3.45) becomes dominant while the thickness ratio term η has minor effect.

Figure 3.16 shows the electric energy generated under the constant curvature condition. The dominance of PVDF-TrFE thickness term in the voltage output also affects the electric energy output. It can be asserted that the electric energy output is proportional to the thickness ratio between the piezoelectric material and the substrate under the constant curvature condition.

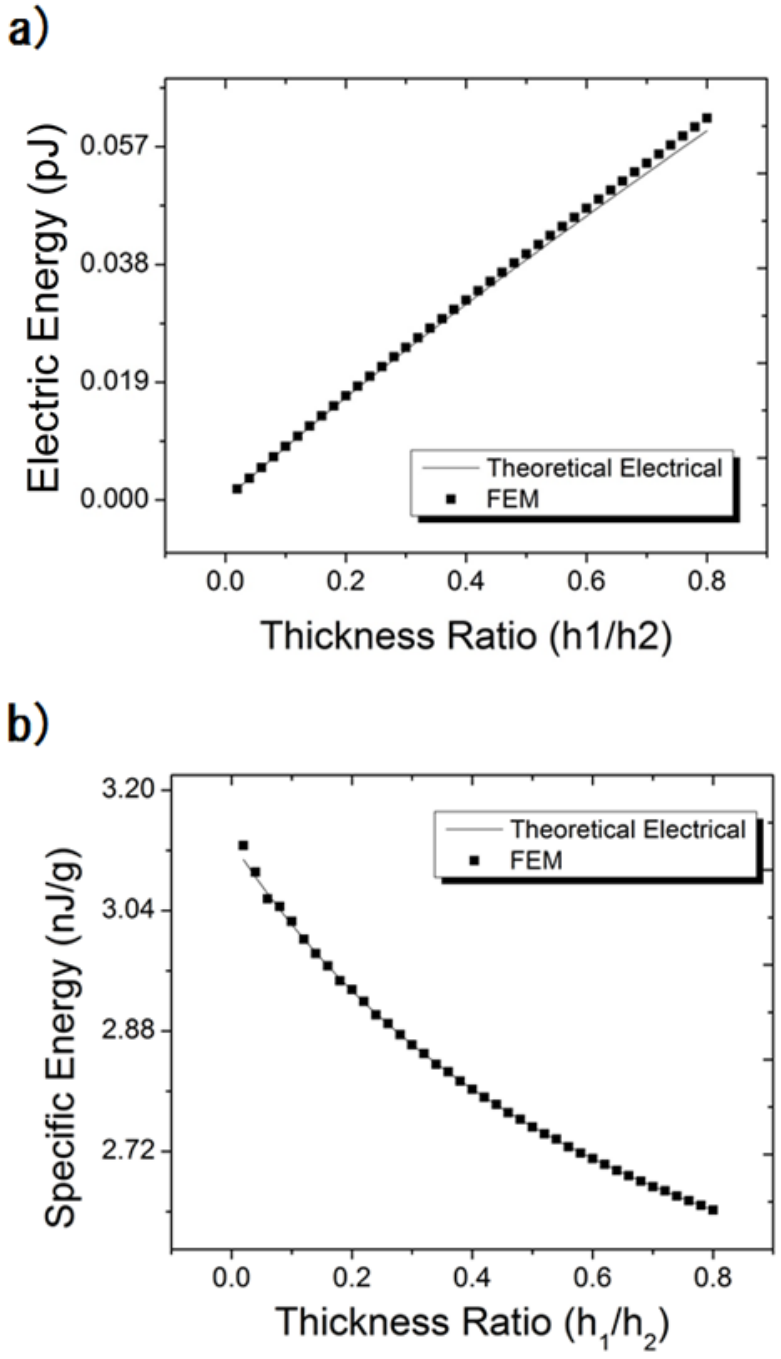

Figure 3.16: a) PVDF-TrFE/Kapton thickness ratio (h_1 / h_2) vs electric energy (J) and b) PVDF-TrFE/Kapton thickness ratio (h_1 / h_2) vs specific electric energy (J/g) under the curvature controlled pure bending condition.

3.5 CANTILEVER BENDING

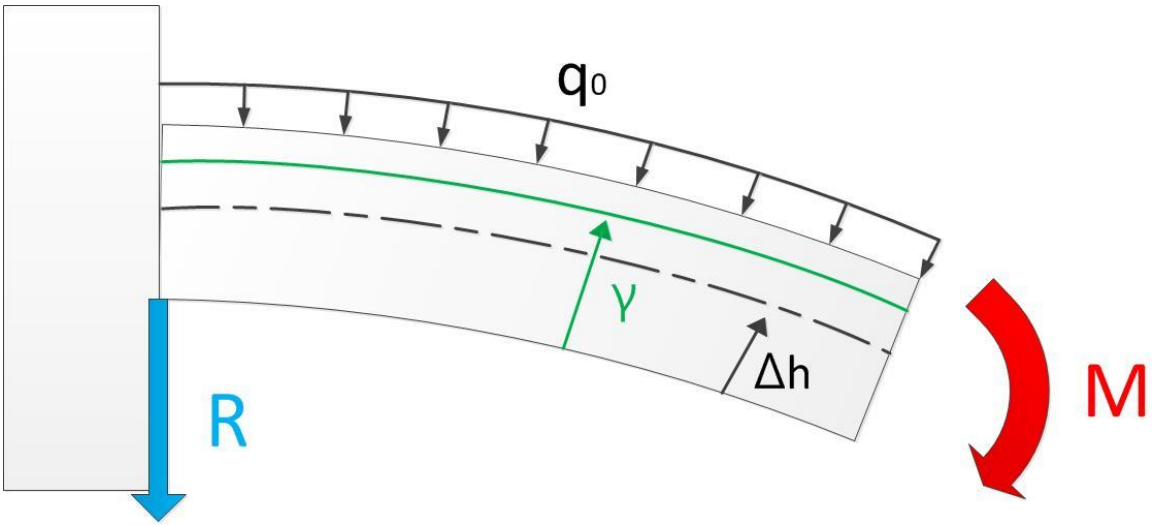

Figure 3.17: A cantilever bending under the uniform loading.

The previous condition of bending was pure bending, which means no load is applied to the structure but the moment. In practical situation, however, various loading conditions exist and affect the structure. Hence, the load term q of the Equation (3.1) is not zero anymore. A generally used structure for the piezoelectric energy harvesting experiment is the cantilever. The boundary condition of the cantilever structure is that one side end is constraint whereas the other side end is free, as depicted in the Figure 3.17. There are many forms of the load boundary condition; in this section, the uniform

loading on the top surface will be discussed. Therefore, the load term q in the Equation (3.1) can be expressed as

$$q(x) = -q_0 \tag{3.46}$$

The negative sign means the loading direction is top-down. The solution of the Equation (3.1) with the uniform loading on the top surface is

$$w = A_1 + A_2 x + A_3 x^2 + A_4 x^3 - \frac{q_0 x^4}{24YI} \tag{3.47}$$

Herein, the boundary condition is applied as mentioned above. For simplicity, the left end(x=0) is fixed and the right end(x=L) is free. The region is different from the pure bending condition depicted in (3.5).

$$x = 0,\ w = \frac{\partial w}{\partial x} = 0 \tag{3.48}$$

$$x = L,\ \frac{\partial^2 w}{\partial x^2} = \frac{\partial^3 w}{\partial x^3} = 0 \tag{3.49}$$

From the boundary condition above, A_1 and A_2 are zero. The Moment M and the shear force R at the left end is

$$x = 0,\ M = \frac{q_0 L^2}{2},\ R = -q_0 L \tag{3.50}$$

for the uniform load condition [22]. In terms of the definition of the direction, the moment is positive (top-tension and bottom-compression) while the shear force is negative. Applying the boundary condition (3.50) to (3.47), the coefficient A_3 and A_4

are $A_3 = -q_0 L^2 / 4YI$ and $A_4 = q_0 L / 6YI$ respectively. As a result, the deflection vector *w* becomes

$$w = -\frac{q_0 x^2 (6L^2 - 4Lx + x^2)}{24YI} \tag{3.51}$$

Unlike the pure bending case, the moment is not uniform along x-axis over the structure anymore. From the Equation (3.51) and the Equation (3.3) which is basic moment-displacement relation, the moment becomes

$$M(x) = \frac{q_0 (L^2 - 2Lx + x^2)}{2} \tag{3.52}$$

The shear force *R*, which is defined as *dM/dx*, can be written as

$$R(x) = -q_0 (L - x) \tag{3.53}$$

However, the shear force is not negligible in our case because of the coupling coefficient given in (3.41). The shear force is applied to the x-z direction of which the subscript numbering is 5. Our case only reckons the thickness direction polarization of which the subscript numbering is 3; there is no coupling coefficient d_{35}.

By substituting the cantilever moment (3.52) into the Equation (3.21) instead of M_0, the longitudinal stress becomes

$$T_{1n} = (\gamma - \Delta h_1) \frac{\overline{Y}_n}{\overline{Y}_2} \frac{q_0 (L^2 - 2Lx + x^2)}{2I}, \; n = 1, 2 \tag{3.54}$$

Consequently, the polarization in the thickness direction from Equation (3.24) is

$$P_3 = d_{31} (\gamma - \Delta h_1) \Sigma \frac{q_0 (L^2 - 2Lx + x^2)}{2I} \tag{3.55}$$

where $h_2 < \gamma < h_1 + h_2$. The charge is the integral of the surface polarization charge density with negative sign in longitudinal direction, which is x. Then the charge on the top and bottom surface become

$$Q_{top} = -\int_S \rho_{ps\_top} ds = W \cdot d_{31} (h_1 + h_2 - \Delta h_1) \Sigma \frac{q_0 L^3}{6I} \tag{3.56}$$

$$Q_{bottom} = -\int_S \rho_{ps\_bottom} ds = -W \cdot d_{31} (h_2 - \Delta h_1) \Sigma \frac{q_0 L^3}{6I} \tag{3.57}$$

Therefore, the equivalent charge and the voltage under the uniform load-cantilever condition are

$$Q_{Equivalent} = LWh_2 \cdot d_{31} \left(1 + \frac{\eta}{2} - \Delta\eta\right) \cdot \Sigma \frac{q_0 L^2}{6I} \tag{3.58}$$

$$V = h_1 h_2 \cdot g_{31} \left(1 + \frac{\eta}{2} - \Delta\eta\right) \cdot \Sigma \frac{q_0 L^2}{6I} \tag{3.59}$$

For the simulation, the right end is fixed as a constraint boundary condition while the right end is free. The symmetry boundary condition and buffer structure are eliminated in this case. The load is applied oh the top; for the same condition to the pure bending condition, $q_0 = 6M_0 / L^2$ is applied where $M_0 = 6.5895 \times 10^{-8}\ N \cdot m$. For the mesh formation, the edge distribution method is used before mapping. With this method, the precise solution can be achieved in COMSOL. From right to left, the length of the mesh segment becomes wider. The number of elements is 20 and the element ratio is 10.

The other parameters such as parametric sweep condition and the mesh size are the same as the pure bending simulation.

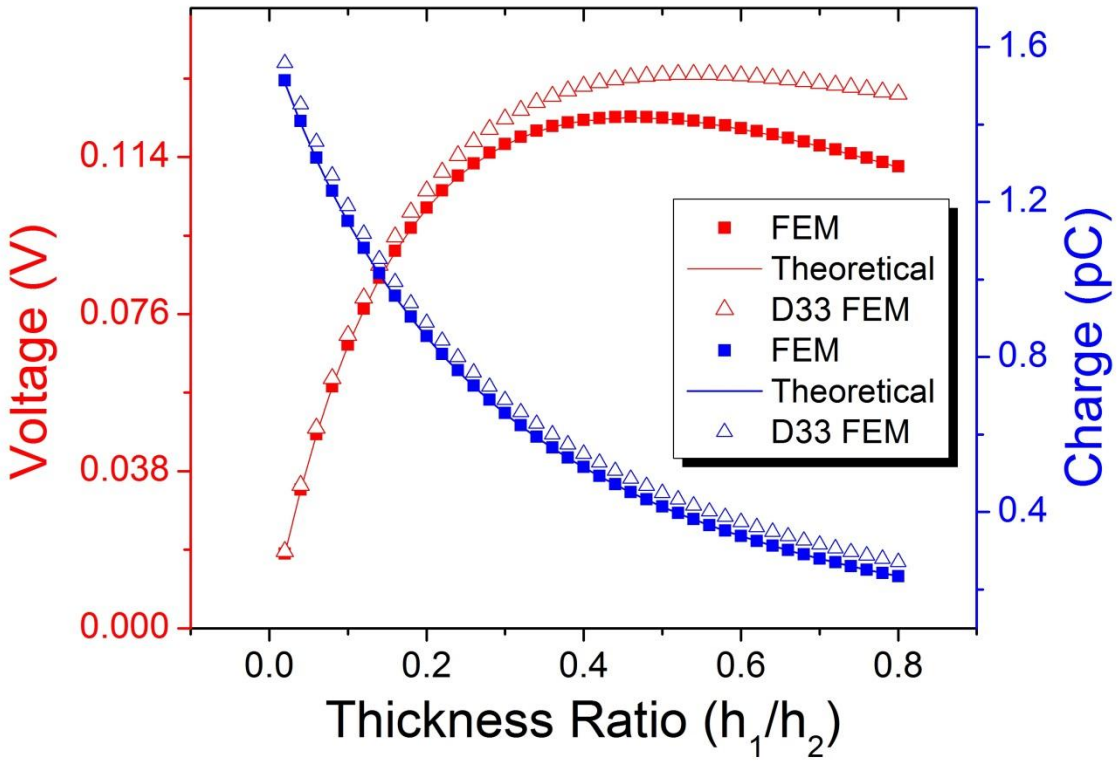

Figure 3.18: PVDF-TrFE/Kapton thickness ratio (h_1 / h_2) vs voltage (V) and charge (C) under the uniform load cantilever bending condition.

Figure 3.18 shows the results of the simulation and the theoretical derivation of the moment controlled, uniform load applied cantilever bending condition. Since the uniform loading is in z-direction, the stress in thickness direction and the coupling coefficient d_{33} are not negligible anymore, compared to the pure bending condition.

D33 FEM shows the result of the cantilever bending output regarding the coupling coefficient d_{33} and the thickness direction stress. Still the d_{31} coupling coefficient and the longitudinal stress are dominant to the electric outputs. FEM is the result excluding the coupling coefficient d_{33}, which matches well with the theoretical derivation.

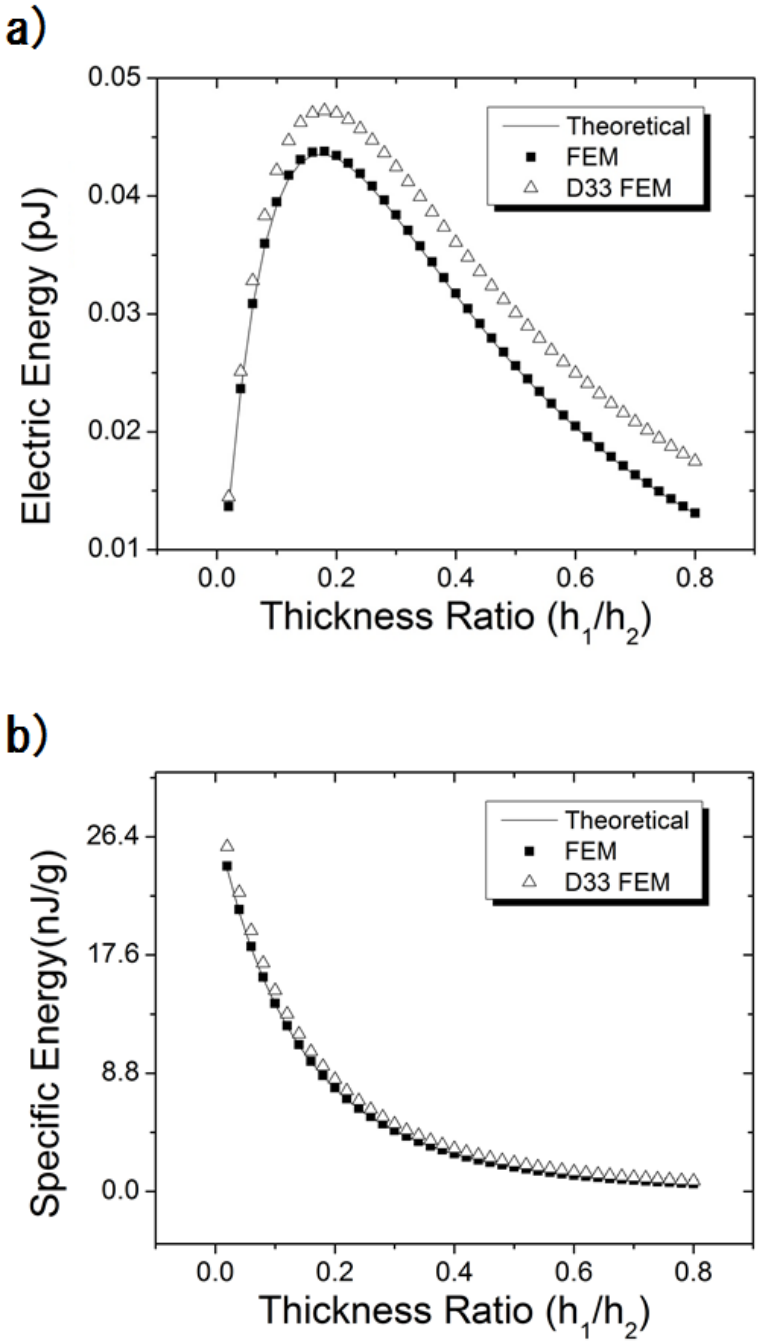

Figure 3.19: a) PVDF-TrFE/Kapton thickness ratio (h_1 / h_2) vs electric energy (J) and b) PVDF-TrFE/Kapton thickness ratio (h_1 / h_2) vs electric specific energy (J/g) under the uniform load cantilever bending condition.

Figure 3.19 describes the electric energy output result of the moment controlled, uniform load applied cantilever bending condition. The difference between the result of D33 FEM and FEM or theoretical derivation is almost constant over the thickness ratio 0.2. This means that the effect of the z-direction polarization generated by the coupling coefficient d_{33} is limited and uncorrelated to the thickness ratio over 0.2. Therefore, the coupling coefficient d_{31} and the longitudinal stress are highly involved in the optimization point of the thickness ratio.

3.6 Effect of Young's Modulus Ratio

The Young's modulus ratio is a parameter which affects the piezoelectric output. Young's modulus of the piezoelectric material is restricted since only few piezoelectric materials are used. Composite piezoelectric material may be an option to manipulate the Young's modulus but hard to expect any orthotropic composite structure effect [39]. Another way to control the Young's modulus ratio is changing the substrate. Selecting an appropriate piezoelectric material, choosing a substrate is comparably easier.

Unlike the thickness ratio, the Young's modulus ratio affects the location of the neutral axis considerably since the Young's modulus ratio can be logarithmically varied. For example from the Guizzetti case, the Young's modulus of the steel substrate was 200GPa whereas that of the piezoelectric material was 20GPa [37]. Assuming the polymer piezoelectric material is coated over the steel substrate, the Young's modulus ratio would be even smaller. The Figure 3.20 shows the effect of the Young's modulus

change with the variation if the thickness ratio. As described, the thickness ratio optimization point varies with the Young's modulus ratio; if the Young's modulus ratio gets larger, the optimization point shifts to the right. Considering the reason of the unimorph/bimorph structure, this becomes obvious [35]. The efficiency of the piezoelectric material will decrease if the neutral axis locates in the piezoelectric material region; the polarization generated by the compression under the neutral axis will cancel out the polarization generated by the tension over the neutral axis. The larger the Young's modulus ratio becomes, the higher the neutral axis locates. Thereby, the unimorph structure that has larger Young's modulus ratio has smaller thickness ratio optimization point. If the circumstance is thickness-limited, the unimorph structure that has higher Young's modulus should be applied and vice versa. Note, the charge also has the thickness ratio optimization point, although it is not significant compared to the voltage.

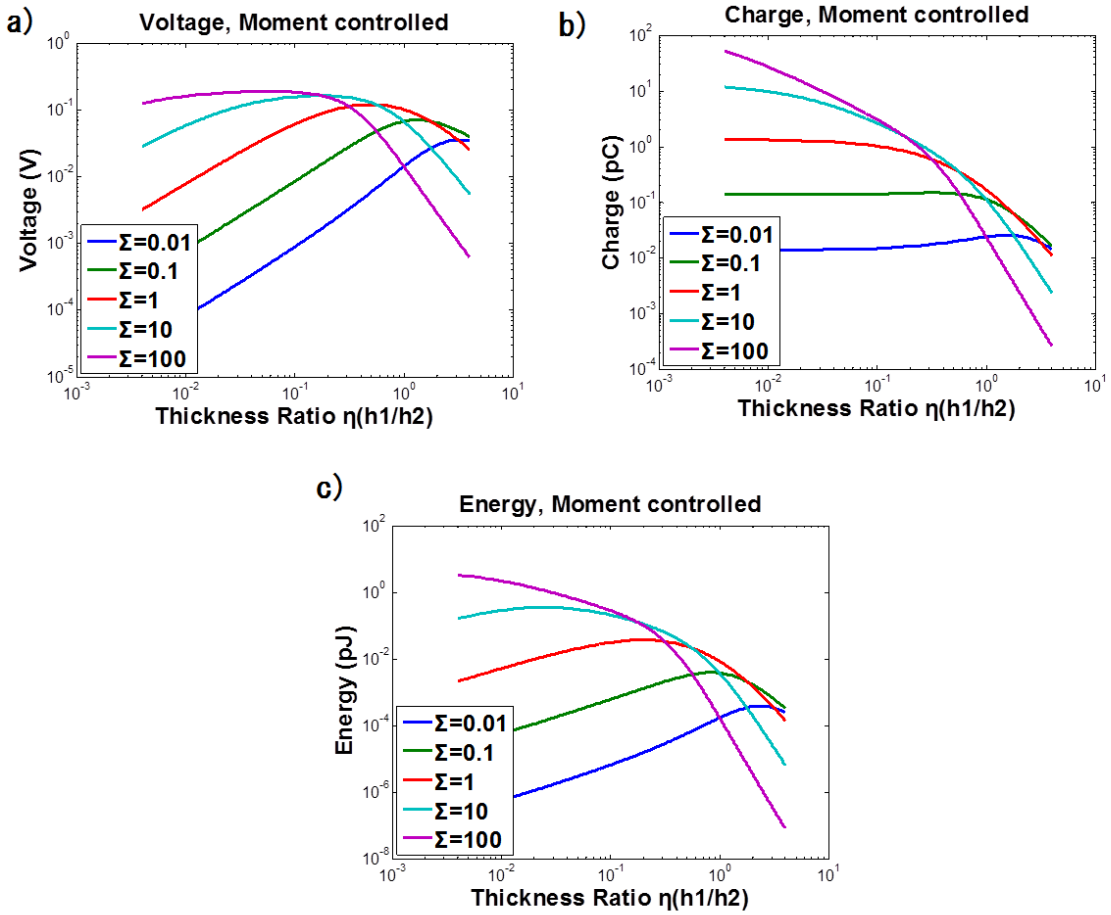

Figure 3.20: PVDF-TrFE/Kapton Thickness Ratio(h_1 / h_2) vs a) Voltage(V) b) Charge(C) c) Electric Energy(J) under Moment Controlled Pure Bending Condition with Varying the Young's Modulus Ratio

Chapter 4 : Numerical Analysis of a Grated Unimorph Piezoelectric Energy HarvesterUnder Pure Bending Condition

In this chapter the structure parameter effect of grated structures are numerically investigated. Herein, the grated structure is defined as periodically spaced stripe-rib structure and only applied to the top surface of the piezoelectric material layer. Firstly, the motivation if the grated structure is asserted, followed by the mechanical analysis. As the real stress distribution is now significantly different from the linear theoretical approach due to the traction free surface and the singularity point. In the third section, the voltage, charge and electric energy output are derived numerically similar to the previous chapter. The base-rib thickness ratio and the rib-spacing ratio affects differently to the electric outputs. Mostly the highest efficiency is achieved by planar structure. As the piezoelectric and the substrate thickness ratio increases, however, the grated structure can be more efficient than the planar structure. Last section covers the structural effect to the piezoelectric coefficient, which suggests the future work of this thesis.

4.1 MOTIVATION

In the last section of the previous chapter, the effect of varying the thickness ratio and the Young's modulus ratio are discussed. Eventually, the purpose of changing the thickness ratio and the Young's modulus is to control the flexural rigidity as well as to control the electric output. The flexural rigidity, especially, is important to biomedical applications since organs are usually very soft and a stiff device attached to

the organs maybe a burden. Therefore, the optimal design with respect to the stiffness and the electric output is a key to build an efficient device.

One way to solve this problem is the porous structure. Many papers suggests that the porous piezoelectric film shows improved result compared to the dense film [40]. The porous processed piezoelectric film such as polypropylene shows the dramatically high coupling coefficient in some cases [41]. However, the increase of the coupling coefficient is related to the chemical spacing during the poling process, not to the mechanical deflection. In addition, the mechanical effect of the porous structure is usually measured as the Young's modulus [41]. Hence, it is hard to say the relation between the stress distribution and the coupling coefficient.

To precise the mechanical effect of the surface porous structure, a 2D porous structure can be estimated with a regularly spaced structure such as the grating structure. The high coupling coefficient created from the grated PVDF-TrFE is already reported [42]. However, the electric output efficiency under a certain mechanical deformation maybe different. For instance, the stress is not applied to the high coupling coefficient region under the certain mechanical deformation, the grated structure is meaningless. On the other hand, if the concentrated stress and the high coupling coefficient region is well matched, higher output efficiency will be expected.

4.2 PREPARATION

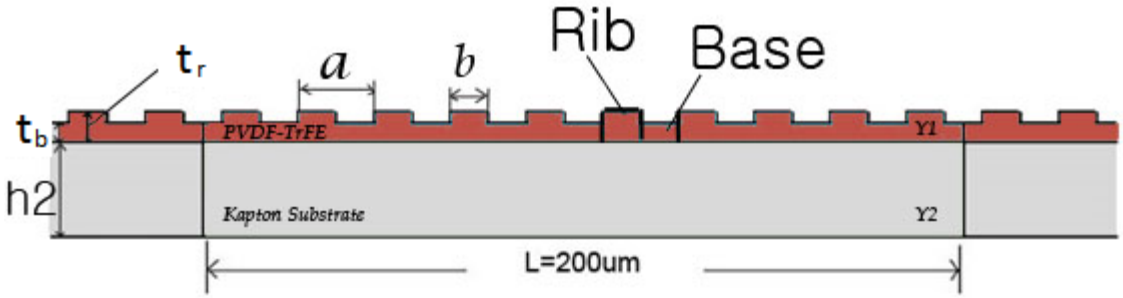

Figure 4.1: A longitudinal section of a grated blanket structure

The grated blanket structure is described in the Figure 4-1. For convenience, the protruding part is called a rib and the rest of the structure is called a base. The base thickness, thereby, is t_b whereas the thickness of the rib is t_r. The length of the rib is *b* and the spacing between ribs is *a*. For the mechanical analysis, the location of the neutral axis is essential. In the grated structure, however, the location of the neutral axis is not flat anymore; it varies with the rib structure as depicted in the Figure 4.2. Also, the location of the neutral axis at a vertical boundary between the rib and the base is not clarified. For simplicity, it is postulated that the neutral axis is discontinuous at the vertical boundary but flat at each region. Therefore, two different neutral axes should be calculated. As described in the Figure 4.2, the neutral axis location of the rib area is $\overline{\Delta t}_r$ whereas that of the base area is Δt_b. For the neutral axis location of the base,

$$\Delta = \frac{1+2\Sigma\eta+\Sigma\eta^2}{2\eta(1+\Sigma\eta)},\ \Delta t_b = Neural\ Axis\ for\ bases \qquad (4.1)$$

where $\eta = t_b / h_2$. For the neutral axis location of the rib,

$$\bar{\Delta} = \frac{1 + 2\Sigma\bar{\eta} + \Sigma\bar{\eta}^2}{2\bar{\eta}(1 + \Sigma\bar{\eta})}, \quad \bar{\Delta}t_r = \textit{Neural Axis for ribs} \tag{4.2}$$

where $\bar{\eta} = t_r / h_2$. In the previous chapter, the Young's modulus ratio is given as $\Sigma = \bar{Y}_1 / \bar{Y}_2$ where $\bar{Y} = Y / (1 - \nu^2)$. Although two different neutral axes are postulated, the connection between two axes lines around the rib and base boundary is not clarified.

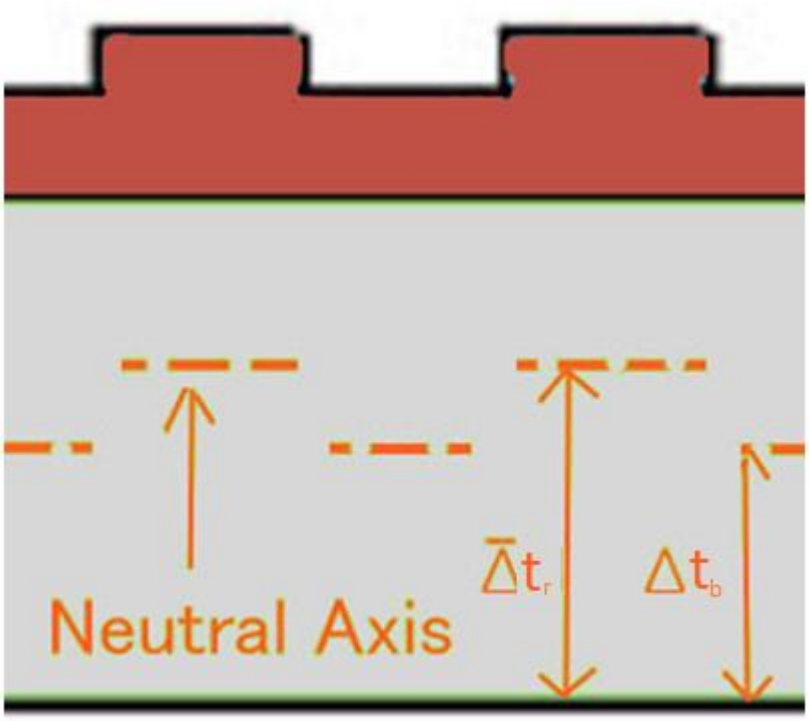

Figure 4.2: A postulation of two different neutral axis locations

The second moment of inertia of each section is also different.

$$I_b = W\left\{\Sigma\frac{t_b^{\,3}}{12} + \Sigma t_b\left(\frac{t_b}{2} + h_2 - \Delta t_b\right)^2 + \frac{h_2^{\,3}}{12} + h_2\left(\Delta t_b - \frac{h_2}{2}\right)^2\right\} \qquad (4.3)$$

$$I_r = W\left\{\Sigma\frac{t_r^{\,3}}{12} + \Sigma t_r\left(\frac{t_r}{2} + h_2 - \overline{\Delta t}_r\right)^2 + \frac{h_2^{\,3}}{12} + h_2\left(\overline{\Delta t}_r - \frac{h_2}{2}\right)^2\right\} \qquad (4.4)$$

For the COMSOL simulation, however, the constant moment is postulated. Therefore, the equivalent second moment of inertia should be applied [43].

$$I_{eq} = \frac{a(I_b \cdot I_r)}{(a-b)I_r + bI_b} \qquad (4.5)$$

Substituting the Equation (4.4) into the Equation (3.6), the new deflection vector *w'* for the grated structure becomes

$$w' = -\frac{M_0}{2YI_{eq}}x^2 \qquad (4.6)$$

where $M_0 = 6.5895\times10^{-8}\ N\cdot m$, as used in the previous chapter. Since the stress and strain distribution is not linear anymore because of the grated structure, the piezoelectric output solution is estimated with the finite element method.

4.3 NUMERICAL ANALYSIS

For the COMSOL simulation, the same material parameters and boundary conditions are used which are mentioned in the Section 3.3 except the two neutral axes, equivalent second moment of inertia and the deflection vector *w'*. The mapped mesh is applied separately in terms of the part; protruding rib parts are meshed with the maximum element size 0.25um and the minimum element size 0.01um while other parts are meshed

with the maximum element size 0.5um and the minimum element size 0.01um. The parametric sweep is used to investigate the effect of grated structure under thickness variation. The thickness of the rib *d* is changed from 2.5 um to 15um with 0.5um for each step, maintaining the ratio of the base-rib thickness t_b / t_r.

There are two parameters that affect the electric outputs; one is the base-rib thickness ratio and the other is rib-spacing length ratio. To estimate the effect of these parameters, different geometry samples are prepared. The samples used in the simulation are suggested in the Table 4.1.

	b:a=10:40 [um]	*b:a* =20:40 [um]	*b:a* =30:40 [um]
t_b / t_r =0.9	G941	G942	G943
t_b / t_r =0.7	G741	G742	G743
t_b / t_r =0.5	G541	G542	G543

Table 4.1: Samples for Numerical Analysis

4.3.1 BASE-RIB THICKNESS RATIO EFFECT

Figure 4.3 shows the result of base-rib thickness ratio variation when the rib-spacing ratio is 20:40 [um]. As can be seen, when the base-rib thickness ratio t_b / t_r decreases, the voltage drops whereas the charge output increases slightly. Compared to the planar structure, the voltage output is reduced while the charge output is improved.

However, the decreasing rate of the voltage output is much larger than the increasing rate of the charge.

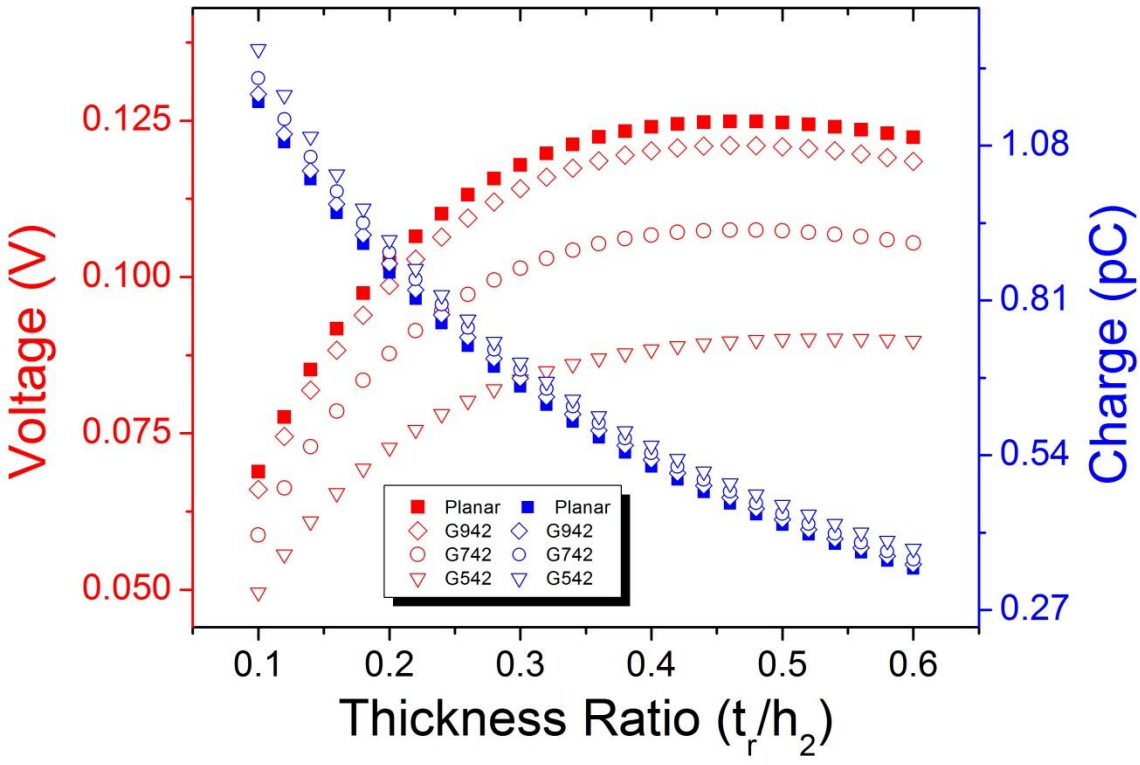

Figure 4.3: Grated PVDF-TrFE/Kapton thickness ratio (t_r / h_2) vs voltage (V) and charge (C) under the moment controlled pure bending condition. The rib-spacing ratio is fixed as 20:40 [um].

Figure 4.4 describes the total energy result of the simulation samples maintaining the rib-spacing ratio *b/a* as 20:40 [um]. The total energy output decreases with respect to the base-rib thickness ratio t_b / t_r. The main reason of the decrement is the inequivalent

compensation between the voltage loss and the charge gain with regard to the base-rib thickness variation.

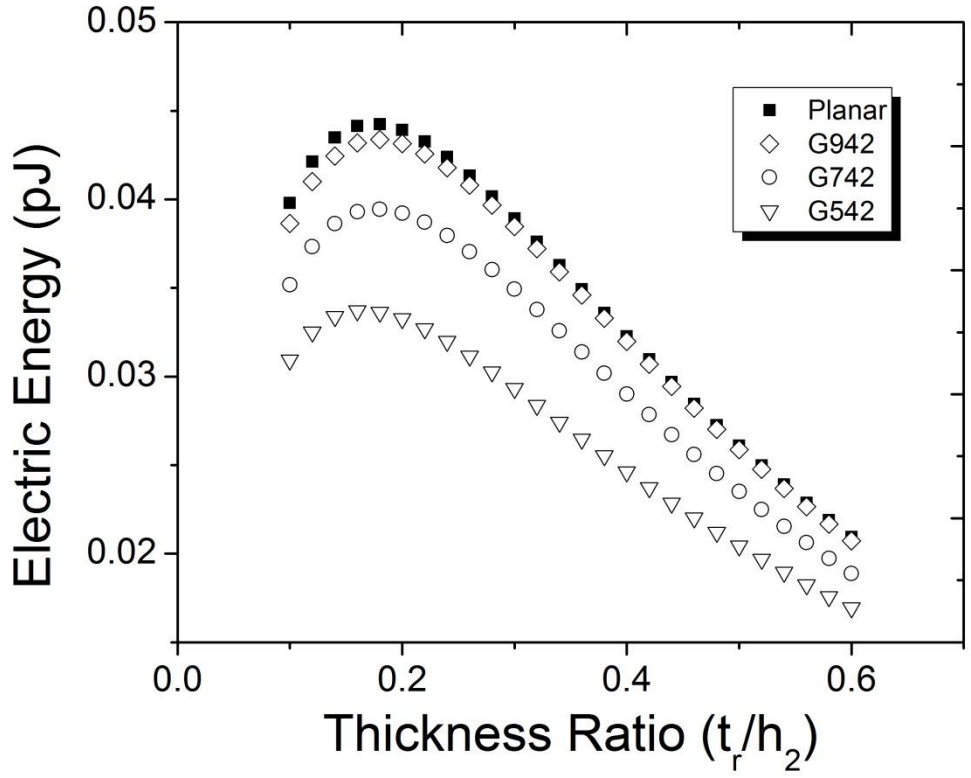

Figure 4.4: Grated PVDF-TrFE/Kapton thickness ratio (t_r / h_2) vs electric energy (J) under the moment controlled pure bending condition**.** The rib-spacing ratio is fixed as 20:40 [um].

Analytically, the voltage output is affected by the thickness manipulation rather than the charge output since the voltage output has the piezoelectric material thickness term which can be observed in the Equation (3.38). Although total thickness is not

changed, the equivalent thickness decreases made by the rib thickness and the base thickness. Therefore, intuitively, the voltage decrease rate is larger than the change increase rate in terms of the grated thickness manipulation.

Another reason of the electric output decrement can be described with the numerical simulation. Figure 4.5 shows the surface stress magnitude of the grated structure. The stress near the base-rib boundary is discontinuous and dramatically diverged. In mechanics, the boundary similar to the rib side wall is called traction-free surface where all stress and strain become zero whereas the peak at the base surface nearest to the rib side wall is called the singularity point. As described with dim color area, the stress loss at the rib surface is wider than the stress gain at the base surface. This loss and gain area expands when the base-rib thickness ratio falls. However, the loss area expansion rate is larger than the gain area expansion rate. Thereby, the total stress loss on the grated surface will increase with respect to the base-rib thickness ratio decrement; consequently, the electric outputs will decrease with respect to the stress-polarization relation in the previous chapter.

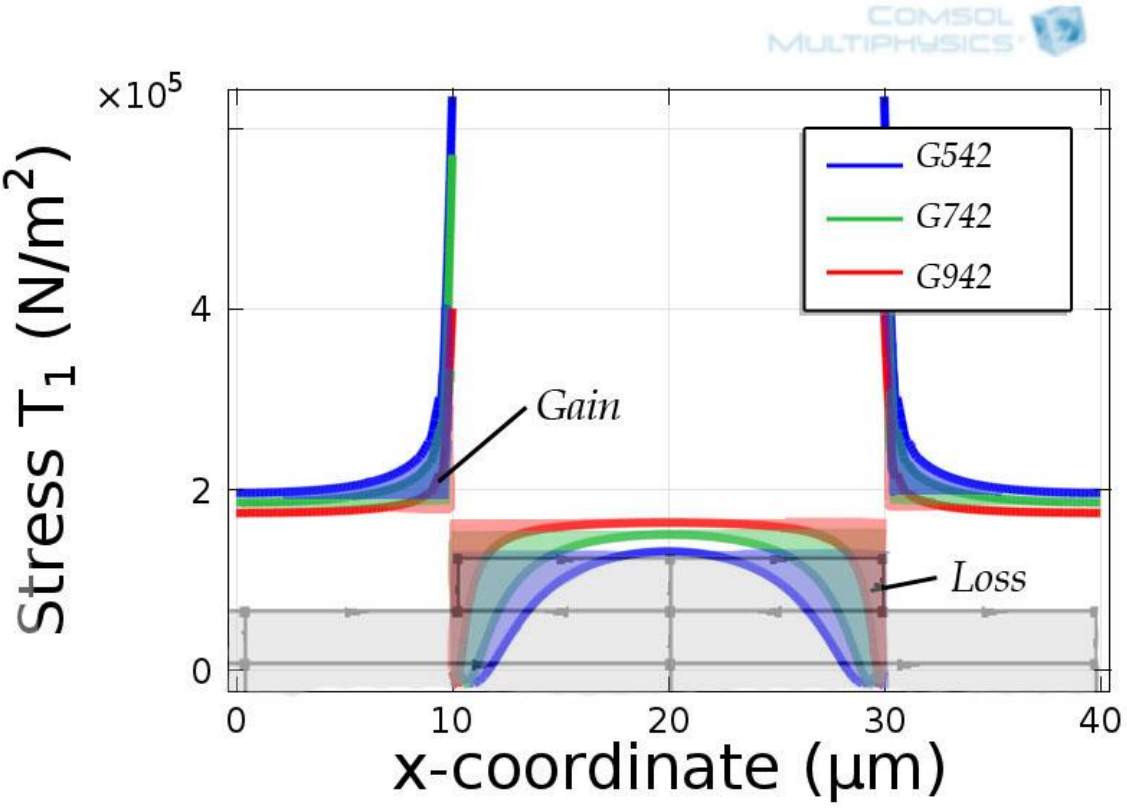

Figure 4.5: Nonlinear surface stress magnitude of the grated structure with respect to the base-rib thickness ratio. The rib-spacing ratio is fixed as 20:40 [um].

4.3.2 RIB-SPACING RATIO EFFECT

Another geometric parameter of grated structure is the rib-spacing ratio *b/a*. The numerical result is shown in the Figure 4.6. Two regions are specified for the voltage output in terms of t_r / h_2; the region before 0.4 and the region after 0.4. The voltage output decreases in the former region and increases in the latter region when the rib-

spacing *b/a* decreases. On the other hand, the charge output increases in all regions when the *b/a* ratio decreases.

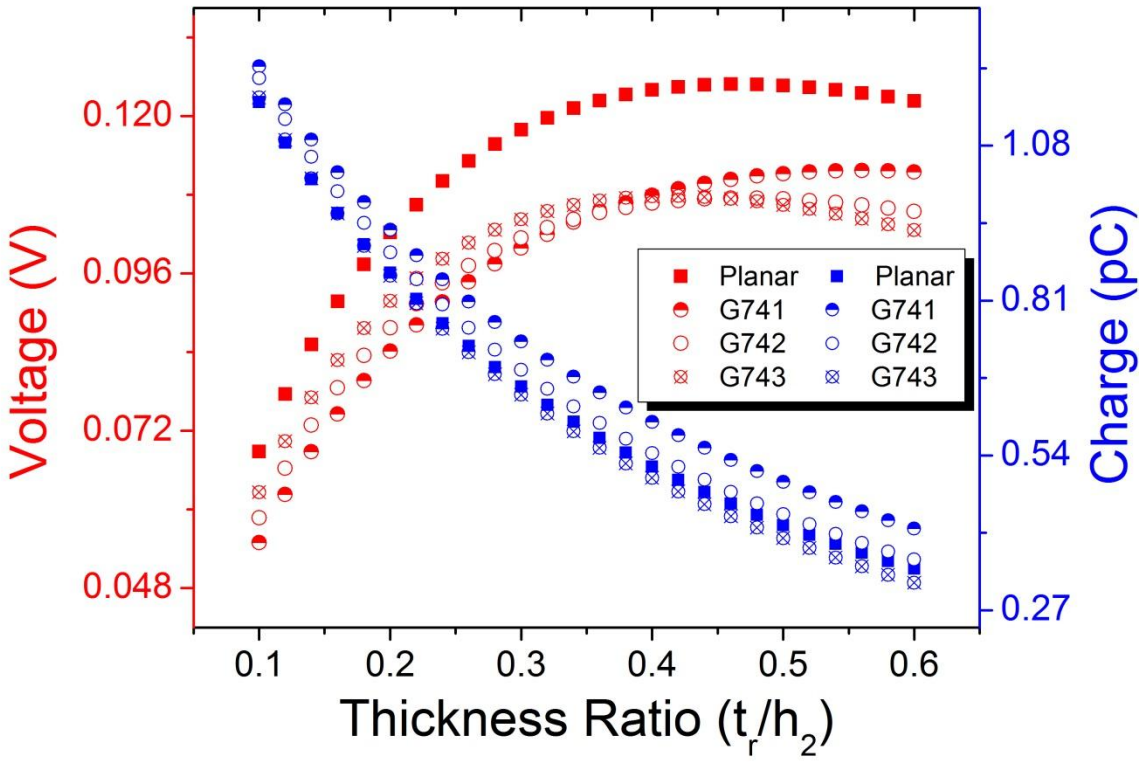

Figure 4.6: Grated PVDF-TrFE/Kapton thickness ratio (t_r / h_2) vs voltage (V) and charge (C) under the moment controlled pure bending condition. The base-rib thickness ratio *h/d* is fixed as 0.7.

Figure 4.7 describes the total energy result of the simulation samples maintaining the base-rib thickness ratio t_b / t_r as 0.7. In the voltage dominant region, the electric energy output decreases when the length ratio decreases. In the charge dominant region, on the contrary, the electric energy output increases when the length ratio decreases. For

G741 sample, the electric energy is even higher than the planar structure where the t_r / h_2 thickness ratio is higher than 0.4.

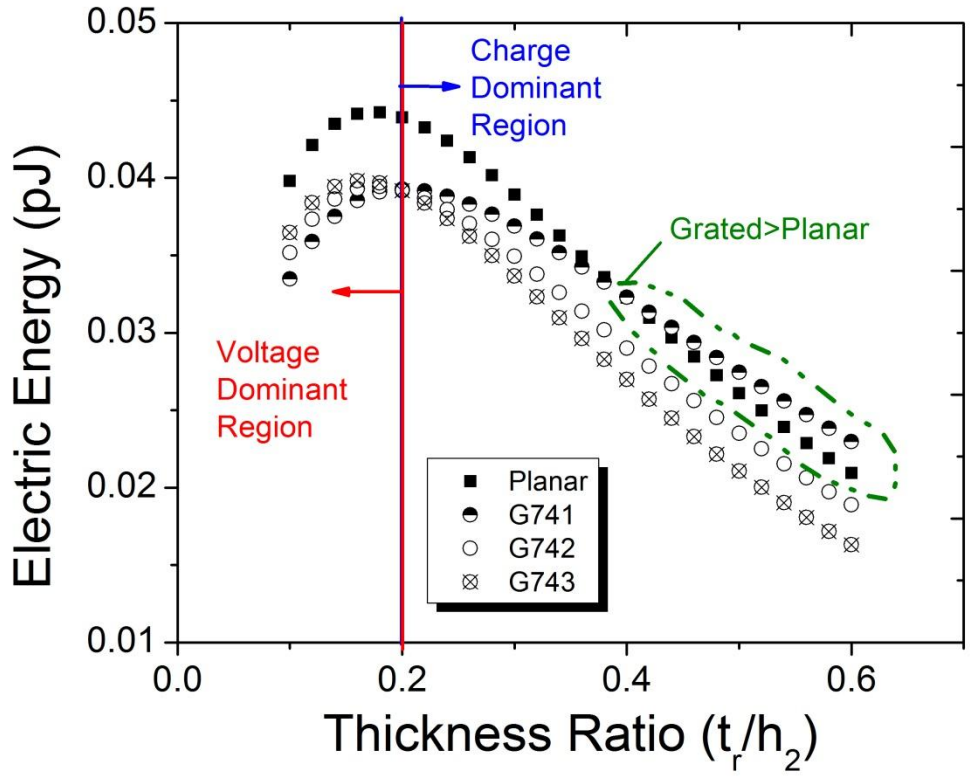

Figure 4.7: Grated PVDF-TrFE/Kapton thickness ratio (t_r / h_2) vs electric energy (J) under the moment controlled pure bending condition**.** The base-rib thickness ratio is fixed as 0.7.

The rib-spacing ratio affects the equivalent second moment of inertia and the equivalent total thickness. If the *b/a* ratio decreases, the second moment of inertia will decrease; hence, the voltage and the charge output will be improved, according to the

Equation (4.5). The equivalent total thickness can be approximated as the same manner of the equivalent second moment of inertia case.

$$h_{eq} = \frac{a \cdot t_b \cdot t_r}{(a-b) \cdot t_r + b \cdot t_b} \qquad (2.1)$$

Accordingly, the equivalent thickness will decrease when the rib-spacing ratio decreases. However, the voltage output decrement rate by *b/a* is not much significant than the voltage output decrement rate by t_b / t_r.

The Figure 4.7 proves that the grated structure is better than the planar structure under specific parameter condition. If the voltage output and the charge output are adequately compensated using the grated structure, high electric output can be achieved. To be specific, if the substrate film thickness is similar to the piezoelectric film thickness, the grated structure will generate more electric output rather than the planar structure.

4.4 STRUCTURAL EFFECT ON PIEZOELECTRIC COEFFICIENT

A recent paper asserts that the piezoelectric coupling coefficient d_{33} increases significantly at singularity points of nanostructure array [42]. At the singularity points, the piezoelectric coupling coefficient d_{33} was ~60 pm/V which is 3 to 20 times higher than the coefficient at the planar surface which is ranging from 3 to 19 pm/V. This result was measured by the Piezoresponse Force Microscopy (PFM). Although only d_{33} is measured in the paper, we can expect that the molecular dipoles are accumulated at the

singularity point. Hence, the piezoelectric coefficient d_{31} will also show similar improvement.

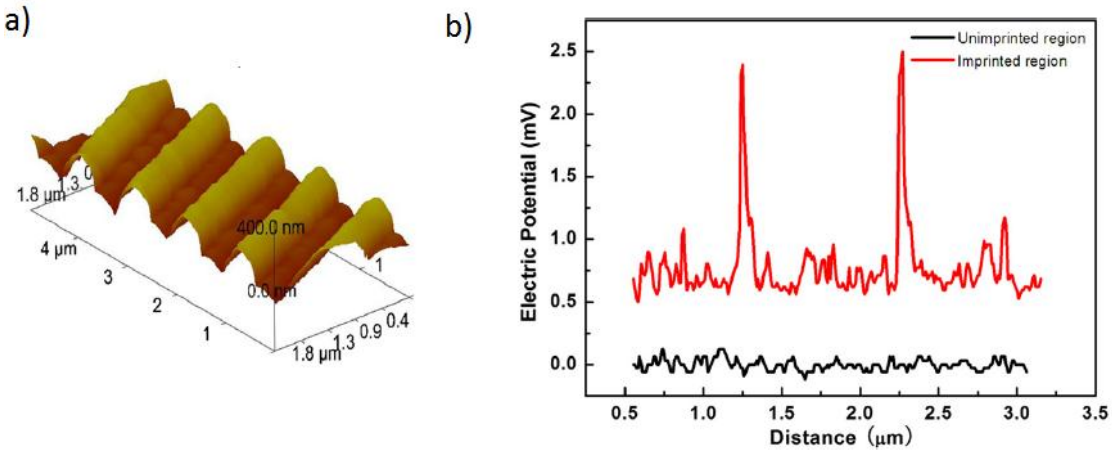

Figure 4.8: a) The nanoimprinted structure suggested by Ran Liu group. The deep is around 350nm. b) The voltage output measured by vertical PFM. The black line is the voltage output from the unimprinted planar area and the red line is the voltage output from the structured area [42].

The results above are measured without external mechanical stimuli. Thereby, the correlation between the Figure 4.5 and the Figure 4.8 b) will suggest the high voltage gain at the singularity point under the moment controlled pure bending condition. Let us consider a grated structure and the diagram in the Figure 4.5; if the voltage gain at the singularity point compensates the voltage loss around the traction-free surface positively, the electric outputs of the grated structure would be better than that of the planar structure. Furthermore, reducing the structure scale or periodicity will enhance the output since the number of singularity per area will increase. Still, the base-rib thickness ratio and the rib-spacing ratio should be considered.

Chapter 5 : Conclusion

In summary, the effect of the thickness ratio variation of a unimorph piezoelectric energy harvester to the electric output under bending condition is investigated. The harvester forms a blanket with a piezoelectric material as upper layer and a substrate material as lower layer. PVDF-TrFE is used as a piezoelectric material whereas Kapton film used as a substrate material. The thickness of Kapton is fixed as 25um while the thickness of PVDF-TrFE is varied from 0.5 um to 20um. The voltage, charge and energy output are calculated with the analytical and numerical method. For numerical calculation, COMSOL simulation is used.

Three bending conditions are suggested; moment controlled condition, curvature controlled condition and uniform-load cantilever condition. The bending condition is fairly considered the practical biomedical application with the modeled moment value. For the moment controlled condition, the voltage and electric energy output have the optimal thickness ratio point while the charge output keeps decreasing. However, if the Young's modulus ratio changes, the charge output also has the optimal thickness ratio point. In addition, the optimal point of all outputs varies with the ratio of the Young's modulus.

Under the curvature controlled condition, the voltage output and the electric energy output increases linearly while the charge output remains almost the same but slightly decreases. The output results under the uniform-load cantilever condition are similar to the output results under the moment controlled condition. However, the effect

of the coupling coefficient d_{33} and the transverse stress T_3 is not negligible anymore compared to the moment controlled condition.

The grated structure effect is investigated with respect to the rib-base thickness ratio and the rib-spacing ratio. The voltage and electric energy output significantly decrease when the base-rib thickness ratio decreases. The charge output increases slightly when the base-rib thickness ratio decreases but the increasing rate is lesser than the decreasing rate of the voltage and electric energy output.

By manipulating rib-spacing ratio, the electric energy output of the grated structure can be improved more than that of the planar structure, if the piezo-substrate thickness ratio is larger than a specific value. Furthermore, a recent research result shows that the piezoelectric coupling coefficient is enhanced around the singularity point of the grated structure where the stress is also concentrated under any bending condition. Therefore, the grated structure would improve the electric energy output of the blanket structured unimorph energy harvester.

In conclusion, this research will support designing optimal thin film biomedical energy harvester.

References

[1] C. Piguet, *Low-power electronics design*. Boca Raton: CRC Press, 2005.

[2] N. S. Shenck and J. A. Paradiso, "Energy scavenging with shoe-mounted piezoelectrics," *Ieee Micro,* vol. 21, pp. 30-42, May-Jun 2001.

[3] J. M. Donelan, V. Naing, Q. G. Li, and Ieee, *Biomechanical Energy Harvesting*. New York: Ieee, 2009.

[4] M. Deterre and Ieee, "MEMS integration for smart medical devices: opportunities and challenges," *2012 Symposium on Design, Test, Integration and Packaging of Mems/Moems (Dtip),* pp. 253-257, 2012.

[5] C. Dagdeviren, B. D. Yang, Y. W. Su, P. L. Tran, P. Joe, E. Anderson*, et al.*, "Conformal piezoelectric energy harvesting and storage from motions of the heart, lung, and diaphragm," *Proceedings of the National Academy of Sciences of the United States of America,* vol. 111, pp. 1927-1932, Feb 2014.

[6] J. C. P. Curie, "Dévelopment, par pression, de l'électricité polaire dans les cristaux hémièdres
à faces inclinées.," *C. R. Acad. Sci.,* vol. 91, pp. 294–295 1880.

[7] J. Tichy, *Fundamentals of piezoelectric sensorics : mechanical, dielectric, and thermodynamical properties of piezoelectric materials*, 1st ed. New York: Springer, 2010.

[8] H. Kawai, "The piezoelectricity of PVDF," *Jpn. J. Appl. Phys.,* vol. 8, pp. 975–976, 1969.

[9] L. Pinna, R. S. Dahiya, F. De Nisi, M. Valle, and Ieee, "Analysis of Self-Powered Vibration-Based Energy Scavenging System," *Ieee International Symposium on Industrial Electronics (Isie 2010),* pp. 402-408, 2010.

[10] H. Allik, K. M. Webman, and J. T. Hunt, "VIBRATIONAL RESPONSE OF SONAR TRANSDUCERS USING PIEZOELECTRIC FINITE-ELEMENTS," *Journal of the Acoustical Society of America,* vol. 56, pp. 1782-1791, 1974.

[11] D. K. Cheng, *Fundamentals of engineering electromagnetics*. Reading, Mass.: Addison-Wesley Pub. Co., 1993.

[12] R. S. Dahiya, *Robotic tactile sensing : technologies and system*, 1st ed. New York: Springer, 2012.

[13] "Introduction to Piezoelectric Actuators and Transducers," International Center for Actuators and Transducers, Penn State University, University Park, PA 168022003.

[14] Y. Jung, *Piezoelectric Energy Harvesting Prospects and Latest Technological Trends*. Seoul, South Korea: Ha-Yeon, 2012.

[15] I. Patel, "Ceramic Based Intelligent Piezoelectric Energy Harvesting Device," in *Advances in Ceramics - Electric adn Magnetic Ceramics, Bioceramics, Ceramics and Environment*, C. Sikalidis, Ed., ed Rijeka, Croatia: InTech, 2011.

[16] P. G. Dineva, D.; Muller, R.; Rangelov, T., *Dynamic fracture of piezoelectric materials*: Springer, 2014.

[17] S. Blackwell, R. Smith, S. D. Kenny, J. M. Walls, and C. F. Sanz-Navarro, "Modelling the growth of ZnO thin films by PVD methods and the effects of post-annealing," *Journal of Physics-Condensed Matter,* vol. 25, Apr 2013.
[18] R. S. Dahiya, L. Lorenzelli, G. Metta, M. Valle, and Ieee, "POSFET Devices Based Tactile Sensing Arrays," *2010 Ieee International Symposium on Circuits and Systems,* pp. 893-896, 2010.
[19] H. S. Nalwa, *Ferroelectric polymers : chemistry, physics, and applications*. New York: M. Dekker, Inc., 1995.
[20] J. K. Yuan, Z. M. Dang, S. H. Yao, J. W. Zha, T. Zhou, S. T. Li*, et al.*, "Fabrication and dielectric properties of advanced high permittivity polyaniline/poly(vinylidene fluoride) nanohybrid films with high energy storage density," *Journal of Materials Chemistry,* vol. 20, pp. 2441-2447, 2010.
[21] R. Tiwari, K. Ryoo, A. Schlichting, and E. Garcia, "Extremely low-loss rectification methodology for low-power vibration energy harvesters," *Smart Materials and Structures,* vol. 22, Jun 2013.
[22] J. M. Gere and B. J. Goodno, *Mechanics of materials*, 7th ed. Toronto, ON ; Clifton Park, NY: Cengage Learning, 2009.
[23] J. E. Shigley, C. R. Mischke, and R. G. Budynas, *Mechanical engineering design*, 7th ed. New York, NY: McGraw-Hill, 2004.
[24] J. W. Hutchinson and Z. Suo, "MIXED-MODE CRACKING IN LAYERED MATERIALS," *Advances in Applied Mechanics, Vol 29,* vol. 29, pp. 63-191, 1992.
[25] J. N. Reddy, *Theory and analysis of elastic plates*. Philadelphia, PA: Taylor & Francis, 1999.
[26] M. A. Meyers and K. K. Chawla, *Mechanical behavior of materials*, 2nd ed. Cambridge ; New York: Cambridge University Press, 2009.
[27] D. Damjanovic, "Ferroelectric, dielectric and piezoelectric properties of ferroelectric thin films and ceramics," *Reports on Progress in Physics,* vol. 61, pp. 1267-1324, Sep 1998.
[28] "Dupont Kapton Polyimide Film General Specifications, Bulletin GS-96-7," E. I. D. Company, Ed., ed. Wilmington, Del., 2011.
[29] V. V. Varadan, Y. R. Roh, V. K. Varadan, and R. H. Tancrell, *MEASUREMENT OF ALL THE ELASTIC AND DIELECTRIC-CONSTANTS OF POLED PVDF FILMS*. New York: I E E E, 1989.
[30] F. P. Beer, *Mechanics of materials*, 6th ed. New York: McGraw-Hill, 2011.
[31] N. R. Cowan, "HEART LUNG COEFFICIENT + TRAVSVERSE DIAMETER OF HEART," *British Heart Journal,* vol. 26, pp. 116-&, 1964.
[32] J. G. Webster and J. W. Clark, *Medical instrumentation : application and design*, 4th ed. Hoboken, NJ: John Wiley & Sons, 2010.
[33] Dieudonn.Jm and C. F. Jean, "EPICARDIAL STRAINS DURING LEFT VENTRICULAR CONTRACTION CYCLE," *American Journal of Physiology,* vol. 216, pp. 1188-&, 1969.

[34] N. N. Rogacheva, *The theory of piezoelectric shells and plates*. Boca Raton: CRC Press, 1994.

[35] R. G. Ballas, *Piezoelectric multilayer beam bending actuators : static and dynamic behavior and aspects of sensor integration*. Berlin ; New York: Springer, 2007.

[36] D. J. Chen, T. Sharma, Y. Q. Chen, X. Fu, J. X. J. Zhang, and Ieee, *Gold Nanoparticles Doped Flexible PVDF-TrFE Energy Harvester*. New York: Ieee, 2013.

[37] V. F. M. Guizzetti, D. Marioli and T. Zawada, "Thickness Optimization of a Piezoelectric Converter for Energy Harvesting," in *COMSOL Conference*, Milan, 2009.

[38] K. W. Kwok, H. L. W. Chan, and C. L. Choy, "Evaluation of the material parameters of piezoelectric materials by various methods," *Ieee Transactions on Ultrasonics Ferroelectrics and Frequency Control,* vol. 44, pp. 733-742, Jul 1997.

[39] J. F. Tressler, S. Alkoy, A. Dogan, and R. E. Newnham, "Functional composites for sensors, actuators and transducers," *Composites Part a-Applied Science and Manufacturing,* vol. 30, pp. 477-482, 1999.

[40] S. Cha, S. M. Kim, H. Kim, J. Ku, J. I. Sohn, Y. J. Park*, et al.*, "Porous PVDF As Effective Sonic Wave Driven Nanogenerators," *Nano Letters,* vol. 11, pp. 5142-5147, Dec 2011.

[41] J. Hillenbrand, G. M. Sessler, Ieee, and Ieee, *Piezoelectric properties of polypropylene/air and poly(vinylidene fluoride)/air composites*. New York: Ieee, 2000.

[42] J. R. Fang, Z. K. Shen, S. Yang, Q. Lu, J. X. Li, Y. F. Chen*, et al.*, "Nanoimprint of ordered ferro/piezoelectric P(VDF-TrFE) nanostructures," *Microelectronic Engineering,* vol. 88, pp. 2033-2036, Aug 2011.

[43] K. Chandrashekhara, *Theory of Plates*. Hyderabad, India: Universities Press (India) Limited, 2001.